Technical Report

ADVANCED COLD X-RAY SOURCE PROGRAM

Approved for public release; distribution is unlimited.

July 2000

Prepared for:
Defense Threat Reduction Agency
45045 Aviation Drive
Dulles, VA 20166-7517

DNA001-93-C-0230

John C. Riordan, et. al.

Prepared by: Maxwell Physics International
P.O. Box 5010
San Leandro, CA 94577-0599

20010420 067

DISTRIBUTION LIST UPDATE

This mailer is provided to enable DTRA to maintain current distribution lists for reports. (We would appreciate you providing the requested information.)

☐ Add the individual listed to your distribution list.

☐ Delete the cited organization/individual.

☐ Change of address.

> **Note:**
> Please return the mailing label from the document so that any additions, changes, corrections or deletions can be made easily. For distribution cancellation or more information call DTRA/ADM (703) 325-1036.

NAME: _____

ORGANIZATION: _____

OLD ADDRESS	**NEW ADDRESS**
_____	_____
_____	_____
_____	_____

TELEPHONE NUMBER: ( ) _____

DTRA PUBLICATION NUMBER/TITLE	**CHANGES/DELETIONS/ADDITIONS, etc.)** *(Attach Sheet if more Space is Required)*
_____	_____
_____	_____
_____	_____

DTRA or other GOVERNMENT CONTRACT NUMBER: _____

CERTIFICATION of NEED-TO-KNOW BY GOVERNMENT SPONSOR (if other than DTRA):

SPONSORING ORGANIZATION: _____

CONTRACTING OFFICER or REPRESENTATIVE: _____

SIGNATURE: _____

CUT HERE AND RETURN

DEFENSE THREAT REDUCTION AGENCY
ATTN: ADM
45045 AVIATION DRIVE
DULLES, VA 20156-7517

DEFENSE THREAT REDUCTION AGENCY
ATTN: ADM
6801 TELEGRAPH ROAD
ALEXANDRIA, VA 22310-3398

REPORT DOCUMENTATION PAGE

1. AGENCY USE ONLY (Leave Blank)	2. REPORT DATE	3. REPORT TYPE AND DATE COVERED
		Technical Report 910828-970331

4. TITLE AND SUBTITLE

Advanced Cold X-ray Source Program

5. FUNDING NUMBERS

C-DNA 001-93-C-0230
PE-4662
PR-AB
TA-AJ
WU-00013

6. AUTHORS(S)

John C. Riordan, P. David LePell, Christopher Deeney, Bruce H. Failor, and Christine A. Coverdale

7. PERFORMING ORGANIZATION NAME(S) AND ADDRESS(ES)

Maxwell Physics International
P.O. Box 5010
San Leandro, CA 94577-0599

8. PERFORMING ORGANIZATION REPORT NUMBER

PIFR-4646

9. SPONSORING/MONITORING AGENCY NAME(S) AND ADDRESS(ES)

Defense Threat Reduction Agency
45045 Aviation Drive
Dulles, VA 20166-7517

NSSS/Schneider

10. SPONSORING/MONITORING AGENCY REPORT NUMBER

DSWA-TR-97-58

11. SUPPLEMENTARY NOTES

This work was sponsored by the Defense Special Weapons Agency under RDT&E RMSS Code
B 4662 D GE 00013 3300 A AB.

12a. DISTRIBUTION/AVAILABILITY STATEMENT

Approved for public release; distribution is unlimited.

12b. DISTRIBUTION CODE

13. ABSTRACT (Maximum 200 words)

This report, the final technical report for the Advanced Cold X-Ray Source Program, describes experimental research efforts to develop plasma radiation sources (PRS) for the simulation of cold x-ray effects. On the Double-EAGLE generator we have investigated four advanced PRS loads: large-diameter aluminum wire array, aluminum/ magnesium wire array, argon/titanium puff-on-wire, and aluminum/titanium wire array. On the Saturn generator we have investigated aluminum/magnesium wire arrays and aluminum/potassium-chloride wire arrays. The large-diameter aluminum arrays demonstrated a K-shell x-ray yield of 50 kJ, a 50% increase over previous results; return current symmetry plays a key role for large diameter implosions. The aluminum/magnesium wire arrays demonstrated a 20% increase in yield over that of pure aluminum; the enhanced yield is due to a combination of opacity and startup effects. The argon/titanium and aluminum/titanium loads both ionized the titanium into the He-like state and produced titanium K-shell x-ray yields of > 1 kJ. For the Saturn experiments, the magnesium/aluminum arrays confirmed the increase in K-shell yield; addition of KCl did not significantly increase the yield above 2.7 keV.

14. SUBJECT TERMS

X-ray Simulator
Wire Array Z-Pinch
Plasma Radiation Source (PRS)
Mixed Element PRS
Puff-on-Wire Z-Pinch

15. PAGE COUNT

75

16. PRICE CODE

17. SECURITY CLASSIFICATION OF REPORT	18. SECURITY CLASSIFICATION OF THIS PAGE	19. SECURITY CLASSIFICATION OF ABSTRACT	20. LIMITATION OF ABSTRACT
UNCLASSIFIED	UNCLASSIFIED	UNCLASSIFIED	SAR

SUMMARY

This is the final technical report for the Advanced Cold X-ray Source Program, prepared by Maxwell Physics International under Defense Threat Reduction Agency contract number DNA001-93-C-0230. During the performance period from 1 October 1993 to 31 March 1997 we have investigated a number of advanced load concepts to improve the x-ray yield and spectral fidelity of plasma radiation sources on Double-EAGLE and Saturn.

Larger-diameter wire arrays increased the aluminum K-shell x-ray yield to 50 kJ, a 50% improvement over the previous optimum yield on Double-EAGLE. The optimum yield was achieved with a 25-mm array, but the yield decreased only slightly for array diameters out to 38 mm. These experiments also demonstrated the importance of wire number and current return symmetry in optimizing the x-ray output.

Mixed-element arrays of aluminum wires containing 20% magnesium as a coating increased the K-shell x-ray yield by 20%, compared to pure aluminum wire arrays of the same mass and diameter. Some of the yield increase is due to the reduction of opacity in the He-like and H-like resonance lines, but the coating dynamics also plays a significant role. Time-resolved spectroscopy showed that the magnesium coating implodes earlier than the aluminum core, creating a hotter plasma on axis.

An argon/titanium puff-on-wire load improved the spectral fidelity by increasing the x-ray yield above 4.5 keV by a factor of four with only a 20% decrease in the total K-shell yield. The best shots produced 1 kJ of titanium x-rays near 4.75 keV and 18 kJ of x-rays above 3 keV. The puff-on-wire load did not achieve the expected high density on-axis because of efficient mixing between the argon and titanium plasmas.

Aluminum/titanium wire arrays provided an alternative source of titanium K-shell x-rays. Arrays of mixed pure wires appeared to perform slightly better than coated wires; a 47% Ti array containing 6 aluminum and 6 titanium wires produced 1.2 kJ of x-rays near 4.75 keV, but only a 15 kJ yield above 1 keV. The titanium coating appeared to produce plasmas that were slightly cooler than those of the puff-on-wire, despite the direct coupling of kinetic energy to the titanium.

Mixed-element wires arrays containing aluminum coated with magnesium or potassium chloride were also tested on Saturn. The addition of a small fraction of magnesium increased the K-shell x-ray yield approximately 20%, but the aluminum/magnesium loads appeared too hot for optimum K-shell x-ray output. The aluminum plasma also radiated a strong free-bound continuum containing more than 35% of the K-shell yield. The potassium chloride coating produced only a slight increase in x-ray yield above 2.7 keV and decreased the combined K-shell yield.

CONVERSION TABLE

Conversion factors for U.S. Customary to metric (SI) units of measurement.

MULTIPLY ⟶ TO GET	BY ⟶ BY	TO GET DIVIDE
angstrom	1.000 000 X E -10	meters (m)
atmosphere (normal)	1.013 25 X E +2	kilo pascal (kPa)
bar	1.000 000 X E +2	kilo pascal (kPa)
barn	1.000 000 X E -28	meter^2 (m^2)
British thermal unit (thermochemical)	1.054 350 X E +3	joule (J)
calorie (thermochemical)	4.184 000	joule (J)
cal (thermochemical/cm^2)	4.184 000 X E -2	mega joule/m^2 (MJ/m^2)
curie	3.700 000 X E +1	* giga becquerel (GBq)
degree (angle)	1.745 329 X E -2	radian (rad)
degree Fahrenheit	$t_k = (t\,°f + 459.67)/1.8$	degree kelvin (K)
electron volt	1.602 19 X E -19	joule (J)
erg	1.000 000 X E -7	joule (J)
erg/second	1.000 000 X E -7	watt (W)
foot	3.048 000 X E -1	meter (m)
foot-pound-force	1.355 818	joule (J)
gallon (U.S. liquid)	3.785 412 X E -3	meter^3 (m^3)
inch	2.540 000 X E -2	meter (m)
jerk	1.000 000 X E +9	joule (J)
joule/kilogram (J/kg) radiation dose absorbed	1.000 000	Gray (Gy)
kilotons	4.183	terajoules
kip (1000 lbf)	4.448 222 X E +3	newton (N)
kip/inch^2 (ksi)	6.894 757 X E +3	kilo pascal (kPa)
ktap	1.000 000 X E +2	newton-second/m^2 (N-s/m^2)
micron	1.000 000 X E -6	meter (m)
mil	2.540 000 X E -5	meter (m)
mile (international)	1.609 344 X E +3	meter (m)
ounce	2.834 952 X E -2	kilogram (kg)
pound-force (lbs avoirdupois)	4.448 222	newton (N)
pound-force inch	1.129 848 X E -1	newton-meter (N•m)
pound-force/inch	1.751 2688 X E +2	newton/meter (N/m)
pound-force/foot^2	4.788 026 X E -2	kilo pascal (kPa)
pound-force/inch^2 (psi)	6.894 757	kilo pascal (kPa)
pound-mass (lbm avoirdupois)	4.535 924 X E -1	kilogram (kg)
pound-mass-foot^2 (moment of inertia)	4.214 011 X E -2	kilogram-meter^2 (kg•m^2)
pound-mass/foot^3	1.601 846 X E +1	kilogram/meter^3 (kg/m^3)
rad (radiation dose absorbed)	1.000 000 X E -2	** Gray (Gy)
roentgen	2.579 760 X E -4	coulomb/kilogram (C/kg)
shake	1.000 000 X E -8	second (s)
slug	1.459 390 X E +1	kilogram (kg)
torr (mm Hg, 0° C)	1.333 22 X E -1	kilo pascal (kPa)

*The becquerel (Bq) is the SI unit of radioactivity; 1 Bq = 1 event/s.
**The Gray (GY) is the SI unit of absorbed radiation.

TABLE OF CONTENTS

FIGURES

FIGURES (Continued)

TABLES

SECTION 1

LARGE DIAMETER ALUMINUM WIRE ARRAYS

The K-shell x-ray output from aluminum wire array plasma radiation sources (PRS) has been explained with reasonable success using one-dimensional models developed by the Naval Research Laboratory Radiation Hydrodynamic Branch (Reference 1). Nevertheless, there is a need to validate these models over a wider parameter range, including larger array diameters. This section describes a set of experiments designed to test these models; the correlation of the experimental data and models will be published elsewhere.

The large-diameter experiments have achieved a number of successes. First of all, we have demonstrated that wire arrays with >30-mm diameters produced stable pinches that are efficient sources of K-shell x-rays; in previous experiments the x-ray yield had decreased dramatically for array diameters above 15 mm. Second, the optimum x-ray yield was increased to 50 kJ, a 50% improvement over the previous optimum yield. Finally, the data indicate the importance of wire number and current return symmetry in optimizing the x-ray performance of wire array PRS.

1.1 WIRE ARRAY LOADS.

For these experiments we used loads with a range of wire array diameters from 15 mm to 40 mm as described in Table 1-1. To investigate the effect of wire number, we used arrays of 12, 18, or 24 wires. In all cases, the arrays were assembled using nominally 100% aluminum wires with diameters ranging from 0.0007 inch to 0.0016 inch to achieve the desired mass. For all shots in this series the wire length was fixed at 20 mm.

Table 1-1. Summary of load parameters for aluminum wire array experiments.

Array Diameter (mm)	Wire Number	Wire Diameter (mil)	Wire Mass (µg/cm)	Moment of Inertia (µg·cm)	Return Diameter (mm)	Gap (mm)	Post Number	Occlusion Factor
15	12	1.2	236	133	22.9	3.9	12	1.38
15	12	1.3	277	156	22.9	3.9	12	1.38
17.5	12	1.3	277	213	25.4	4.0	12	1.44
17.5	12	1.5	369	283	25.4	4.0	12	1.44
17.5	12	1.6	420	322	25.4	4.0	12	1.44
22	24	1.0	328	397	35.1	6.5	12	1.82
25.5	18	1.0	246	400	35.1	4.8	12	1.82
27.5	24	0.8	210	397	35.1	3.8	12	1.82
32	24	0.7	161	412	50.0	9.0	12	2.65
38	24	0.7	161	581	50.0	6.0	12	2.65
40	24	0.8	210	840	50.0	5.0	12	2.65

The number of current return posts in these experiments was increased from six to twelve to improve the symmetry for large diameter arrays. In most wire array PRS experiments the radial gap between the wire array and the current return array is set at 4 to 5 mm (regardless of the array diameter) to minimize load inductance and avoid gap closure. For large diameter arrays, however, the small radial gap places some wires close to the magnetic minima between adjacent current return posts, causing significant asymmetry in the magnetic (JxB) forces acting on the wires. Doubling the number of return posts will greatly improve the magnetic field symmetry, as discussed later in this section.

The load hardware was completely redesigned to incorporate a number of other improvements. Figure 1-1 illustrates the load hardware for a typical wire array diameter of 25.5 mm. To improve power flow in the final convergence before the load, we redesigned the conical surfaces on the cathode cone and top hat. To improve the current contacts for the high current density near the load, we have also redesigned the current gaskets (stainless steel on the cathode cone shank and RG-223 braid under the return cage). Manufacturing and assembly tolerances were also reduced to assure better symmetry.

1.2 DOUBLE-EAGLE CIRCUIT MODEL.

The wire arrays were imploded on the Double-EAGLE generator operated with the Marx bank charged to 60 kV. The load current rose with a linear slope of approximately 50 MA/μs and reached a peak current of 4 to 5 MA depending upon the load. Typical load current and x-ray waveforms are shown in Figure 1-2. The implosion time (defined as the time between baseline intercepts of linear fits to the current ramp and the leading edge of the x-ray pulse) ranged from 80 to 116 ns.

In correlating the measured implosion times and currents with the array masses, we found it necessary to modify the Double-EAGLE circuit model to that shown in Figure 1-3a. The primary change is a reduction in inductance, which is now in better agreement with geometric inductance calculations. Figure 1-3b shows that the revised circuit model provides good agreement for current waveforms with both short circuit and wire array loads.

Figure 1-4 compares the measured implosion times and peak currents with those predicted by the revised Double-EAGLE circuit model using a zero-dimensional slug model for the imploding load (Reference 2). The data are plotted as a function of the load moment of inertia (mr^2), which determines the implosion time and kinetic energy coupling in a slug-model implosion. In general
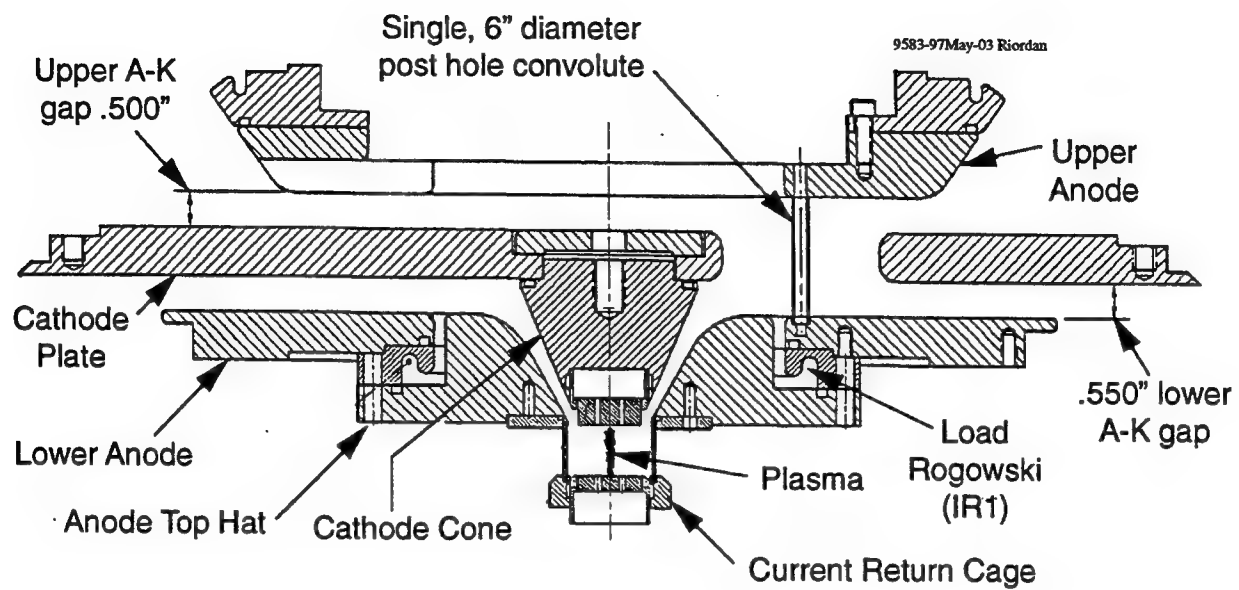
Figure 1-1. Load hardware for 25.5-mm-diameter wire array.
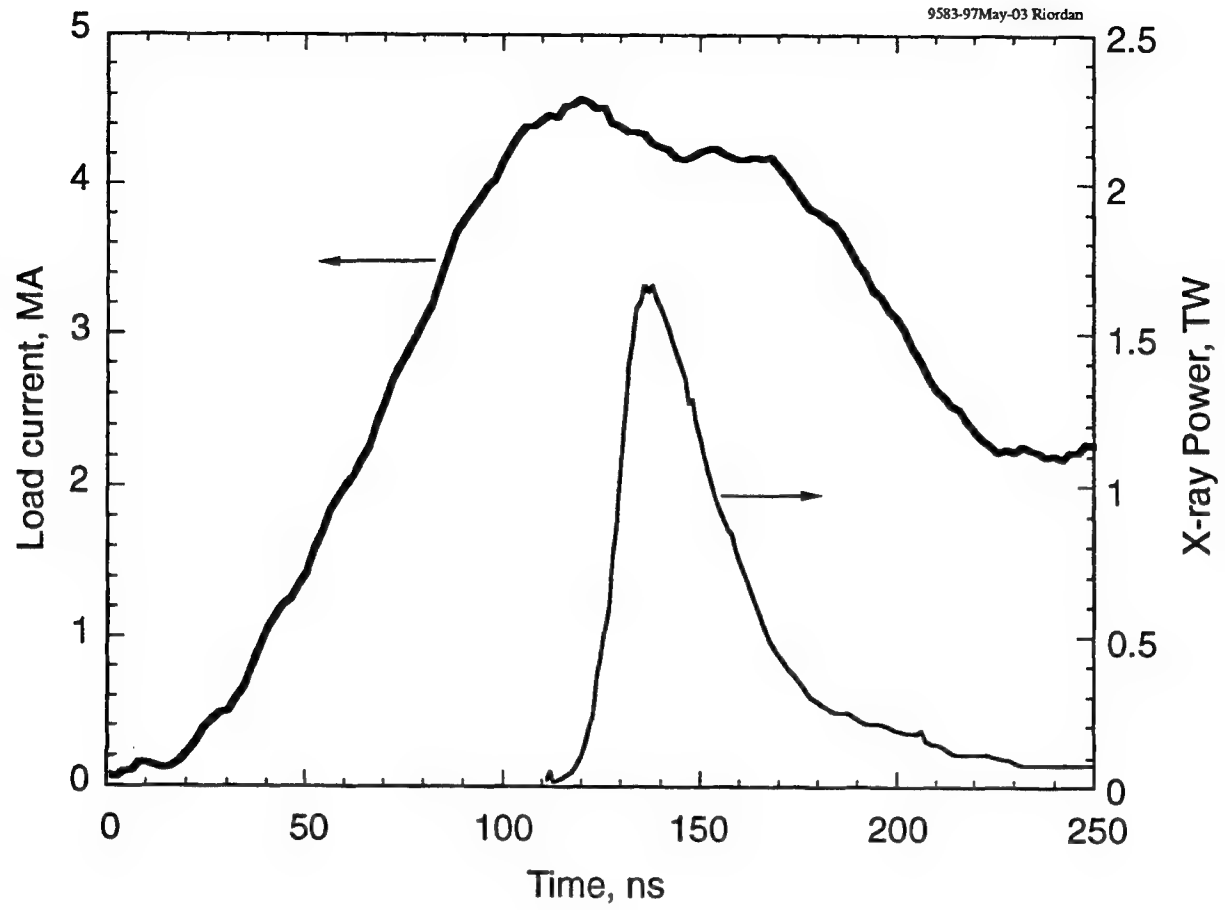
Figure 1-2. Typical load current and x-ray waveforms.

(a)

$$0.3\,\Omega \qquad 20\ \text{nH}$$

$$V_{oc} \qquad L_0 = 5\ \text{nH}$$
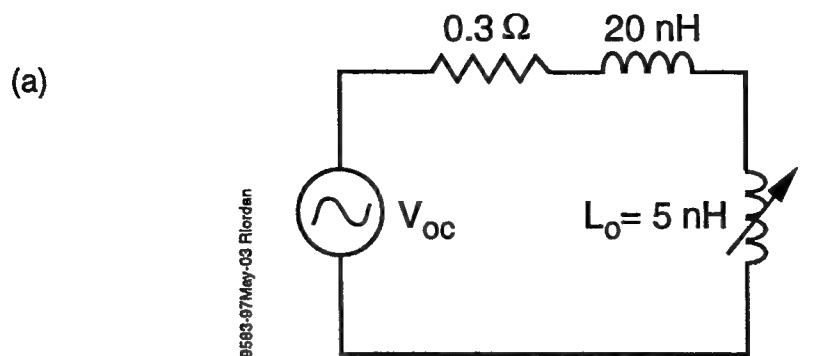
$$V_{oc} = 2.35\ \text{MV} \left(1 + \left(\frac{t}{320}\right)^2\right) \sin\frac{\pi t}{160}$$

$$t \sim \text{ns}$$

(b)
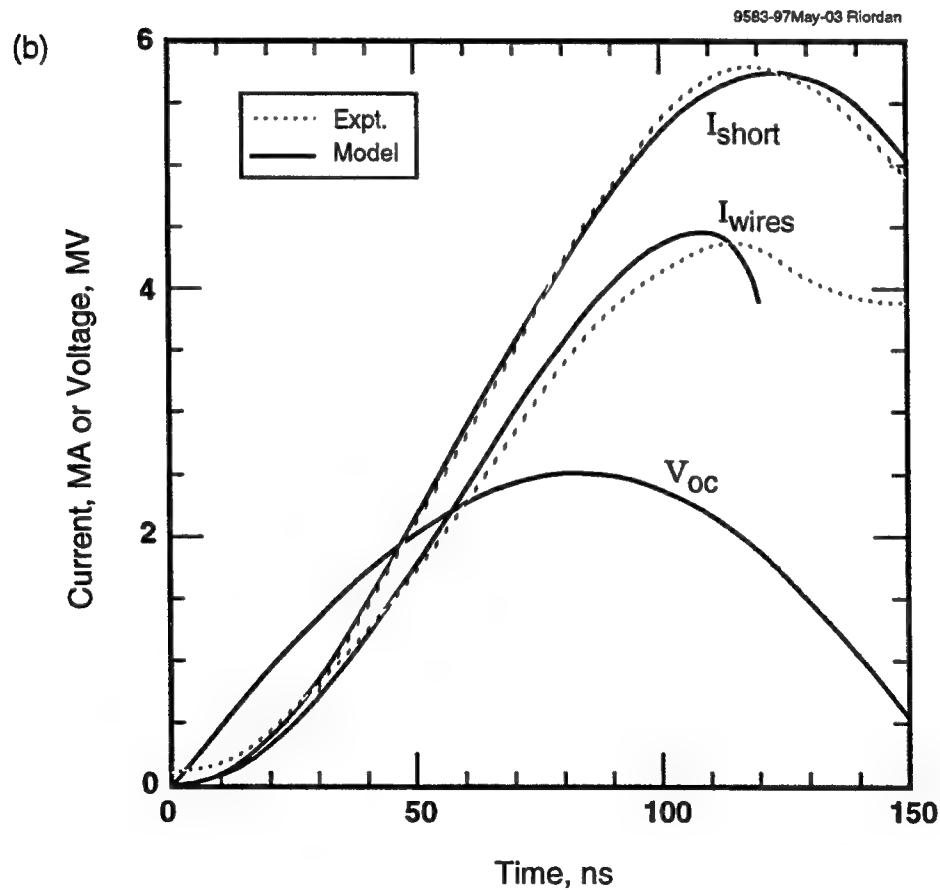
Figure 1-3. Zero-dimensional (slug) model for wire array implosions; (a) Double-EAGLE circuit; (b) load current and open-circuit voltage waveforms.

a)

Current, MA

At Peak

When r/r₀ = 0.1

b)

Implosion time, ns

Theory
● Al (≥94%)
○ Al/Mg

Moment of inertia mr_o^2, μg-cm
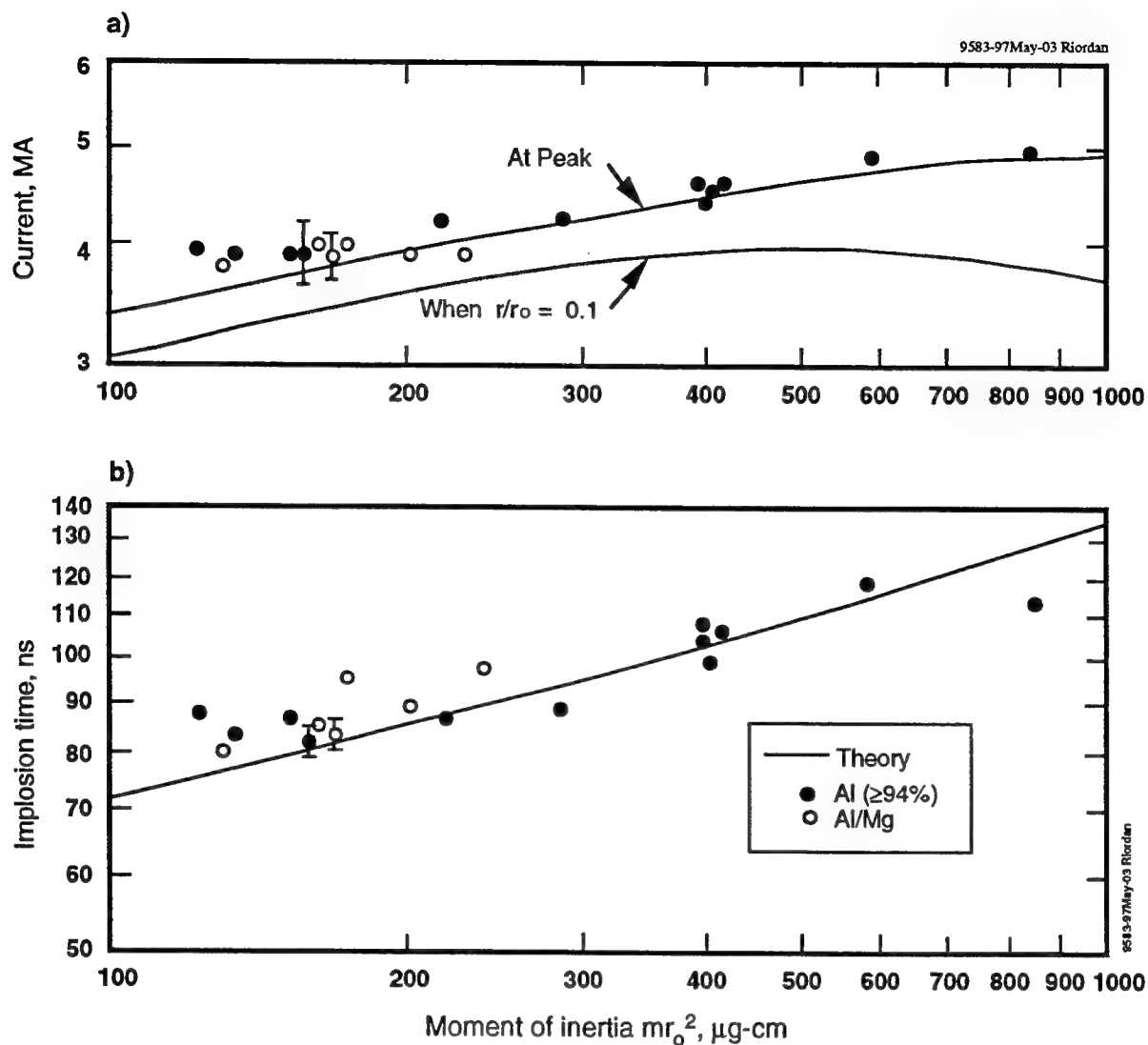
Figure 1-4. Comparison of measurements and theoretical predictions from a zero-dimensional model; (a) load current and (b) implosion time.

the theoretical curves provide an excellent fit to the data except for loads with low moment of inertia, which implode later and reach higher peak currents than predicted.

1.3   X-RAY MEASUREMENTS.

X-ray diagnostics were fielded to measure the aluminum K-shell yield, power, and spectrum, as well as x-ray images of the emitting aluminum plasma. The x-ray yield and power diagnostics consisted of a pair of 7.5-μm tantalum calorimeters and a pair of 0.5-mm diamond photo-conductive detectors (PCDs), respectively. All of these detectors are thick enough for complete absorption of the aluminum K-shell x-rays. To eliminate any response to sub-keV radiation, the calorimeters and PCDs were filtered with thin plastic films. The calorimeter filter consisted of 8.5-μm Kapton plus 2.1-μm Kimfol, while a 8.5-μm Kapton plus 2.1-μm Mylar filter was used for the PCDs. We also fielded a copper x-ray diode (XRD) filtered with 8.5-μm Kapton to provide additional pulse width data; the calibration of the XRD is not reliable enough to be used for absolute power measurements.

In converting the calorimeter and PCD signals into an equivalent isotropic yield, we have corrected for line-of-sight occlusion and filter transmission. An exact filter correction requires a spectrally-weighted transmission factor based upon the measured K-shell x-ray spectrum. Examination of typical spectra show that >95% of the x-ray yield is nearly evenly divided between the He-α and H-α lines at 1.60 and 1.73 keV, respectively. Thus, we have used average transmission factors (at 1.67 keV) of 0.40 and 0.38, respectively, for the calorimeter and PCD filters. The error introduced by use of the average transmission is estimated at <5%. The occlusion factor results from the fact that the diagnostic lines of sight are inclined at 67 degrees to the source axis (rather than perpendicular). In this situation the current return cage obscures the end of the PRS plasma farthest from the cathode cone (Figure 1-1). The line-of-sight occlusion factors are given in Table 1-1 and clearly increase for larger diameter cages.

Table 1-2 presents the x-ray, current, and load data for the entire set of aluminum wire arrays. We have excluded several shots where Double-EAGLE failed to deliver a good current pulse to the load, either because of an arc in the vacuum power feed or poor synchronization (>20 ns) of the north and south pulses. The calorimeter and PCD yield data columns each represent the average of a pair of nominally identical detectors. Within each pair the data usually agree within about 5%, but the PCDs and calorimeters typically differ by about 10%. The PCD waveforms show longer pulse widths than the XRDs and also show a long tail not observed in the XRDs. We suspect that relaxation processes in the PCDs may distort the measured pulse shape.

7

Table 1-2. Summary of experimental data for aluminum wire array experiments.

Shot No.	Array Diam. (mm)	Wire No.	Wire Mass (μg/cm)	Implosion Time (ns)	Peak Current (MA)	Linear dI/dt (MA/μs)	Calorim. Yield (kJ)	PCD Yield (kJ)	PCD FWHM (ns)	XRD FWHM (ns)
3066	15	12	236	84	3.9	46	37.8	39.1	37	-
3067	15	12	236	-	-	-	31.2	31.1	23	-
3069	15	12	236	80	4.0	48	40.3	38.8	40	26
3070	15	12	236	75	3.7	51	34.4	39.3	40	32
3073	15	12	236	-	-	-	38.6	44.7	34	30
3076	15	12	236	85	3.8	46	39.5	42.8	29	26
3149	15	12	277	86	3.9	46	24.7	30.9	32	26
3150	15	12	277	82	3.7	50	35.2	38.6	46	32
3159	15	12	277	80	4.3	47	28.2	30.6	32	26
3160	15	12	277	80	3.7	44	30.2	36.7	24	20
3161	15	12	277	-	-	-	35.3	36.4	40	36
3168	17.5	12	277	82	4.3	49	37.0	35.9	35	34
3170	17.5	12	277	88	4.2	51	39.7	33.3	35	28
3171	17.5	12	369	91	4.1	52	35.6	34.7	42	42
3172	17.5	12	369	85	4.3	52	45.2	43.9	41	38
3173	17.5	12	420	-	-	-	32.4	30.7	44	36
3152	22	24	328	108	4.4	49	28.9	32.2	26	20
3153	22	24	328	108	4.4	51	34.8	37.9	30	26
3141	25.5	18	246	98	4.6	56	50.4	48.0	33	24
3142	25.5	18	246	101	4.5	51	50.4	50.8	40	30
3154	27.5	24	210	102	4.6	54	31.5	29.3	22	18
3155	27.5	24	210	102	4.6	56	31.5	37.1	27	24
3143	32	24	161	-	-	-	28.6	28.4	17	16
3144	32	24	161	106	4.6	51	29.2	26.8	19	18
3145	38	24	161	116	5.0	56	27.3	25.2	22	20
3146	38	24	161	112	4.8	52	23.9	27.6	24	22
3157	40	24	210	115	5.0	56	22.8	29.7	35	-
3158	40	24	210	113	5.0	58	20.1	28.9	47	46

1.4 YIELD SCALING WITH DIAMETER.

To proceed with the analysis, we have taken the data of Table 1-2 and averaged over all shots with nominally identical loads. Mean values for the data are presented in Table 1-3; standard deviations are also calculated for the x-ray yield and pulse width. The x-ray yield is the average of the calorimeter and PCD data, while the x-ray pulse width refers to an average of the PCD and XRD data. The average yields are plotted against wire array diameter in Figure 1-5. The closed symbols
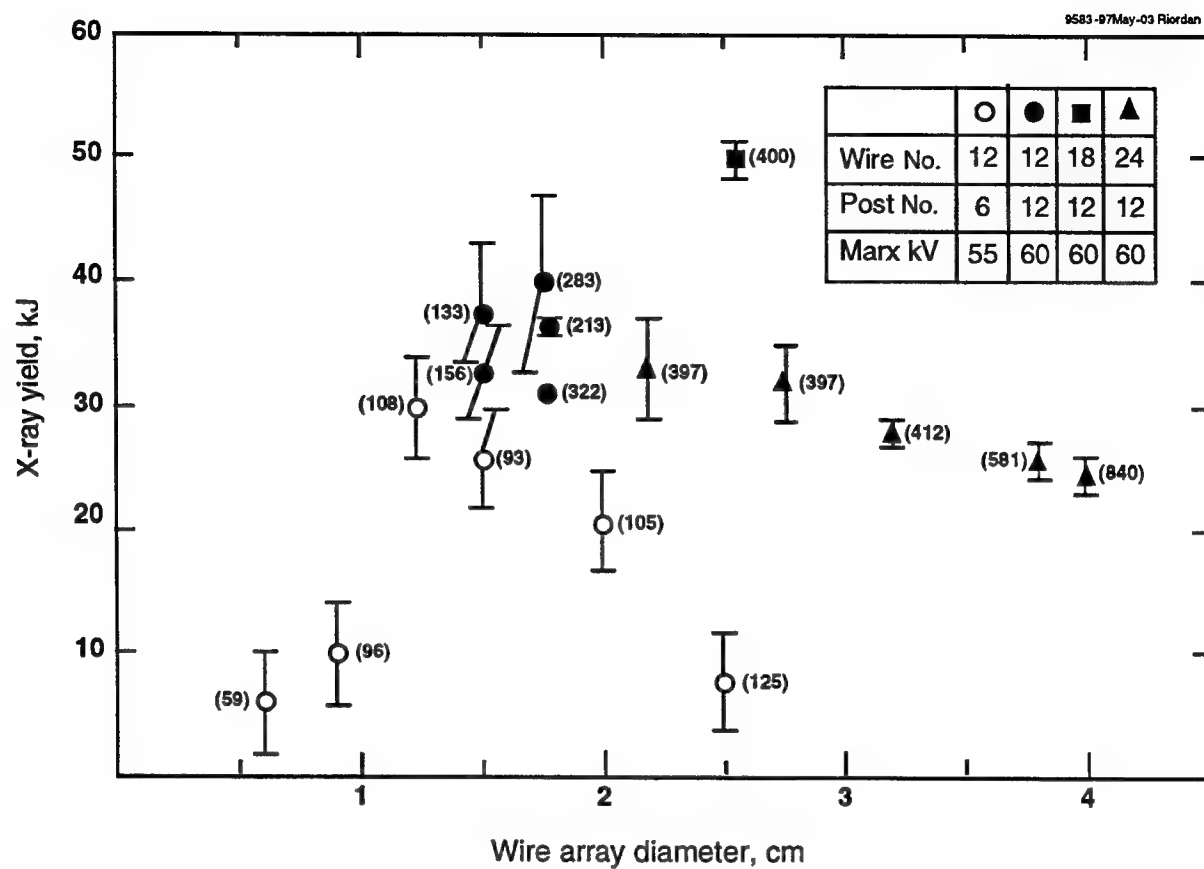
Figure 1-5. Aluminum K-shell yield versus wire array diameter; number in parentheses is the array moment of inertia in μg-cm.

9

represent the present experiments, while open circles represent results from earlier experiments discussed below. Different symbols represent differences in the number of wires in the array. The number in parentheses next to each data point is the moment of inertia, which determines the kinetic energy coupled to the load. Several important conclusions can be drawn from this data.

Table 1-3. Averaged data for aluminum wire array experiments.

Array Diam. (mm)	Wire No.	Wire Mass (μg/cm)	Moment of Inertia (μg·cm)	Implosion Time (ns)	Peak Current (MA)	X-ray Yield Mean ± St. Dev. (kJ)	X-ray FWHM Mean ± St. Dev. (ns)	No. of Shots
15	12	236	133	81	3.9	38.1 ± 3.9	31 ± 5	6
15	12	277	156	82	3.9	32.9 ± 4.2	31 ± 7	5
17.5	12	277	213	85	4.3	36.5 ± 0.1	33 ± 2	2
17.5	12	369	283	88	4.2	39.8 ± 6.8	41 ± 2	2
17.5	12	420	322	-	-	31.5 ± na	40 ± na	1
22	24	328	397	108	4.4	33.5 ± 4.0	26 ± 4	2
25.5	18	246	400	100	4.6	49.9 ± 1.0	32 ± 5	2
27.5	24	210	397	102	4.6	32.4 ± 2.8	23 ± 4	2
32	24	161	412	106	4.6	28.3 ± 0.4	18 ± 1	2
38	24	161	581	114	4.9	26.0 ± 0.4	22 ± 2	2
40	24	210	840	114	5.0	25.4 ± 1.2	41 ± 8	2

First of all, the wire number appears to play a major role in determining the x-ray yield. Consider the wire arrays with diameters of 22, 25.5, 27.5 and 32 mm, which were designed with moments of inertia of nearly 400 μg-cm to produce a 100-ns implosion. Previous experiments have shown that this implosion time provides near optimum kinetic energy coupling on Double-EAGLE. The x-ray yields for the 22-, 27.5-, and 32-mm arrays are approximately 30 kJ; the 25.5-mm array, however, produces a 49-kJ yield that exceeds its neighbors by several standard deviations. The 25.5-mm array differs from the other three arrays in that it contains only 18 wires rather than 24. Because of the flatness of the yield curve through the other three diameters, we believe that the peak yield at 25.5-mm diameter does not represent an optimum diameter, but rather a near-optimum number of wires. Additional evidence for wire number effects is described in Section 2. Sanford (Reference 3) has also observed effects of wire number variation in Saturn wire arrays and attributes these effects to the merging of individual wire plasmas into a cylindrical shell.

Secondly, the present data show that the yields hold up fairly well for large diameter arrays. Thus, our present results are in disagreement with 1989 experiments (Reference 4), which showed a five-fold reduction in yield as the array diameter doubled from 12.5 to 25 mm; the 1989 data are plotted as open circles in Figure 1-5. Although the Marx charge voltage was 9% higher in the present experiments, this would only explain a 20% increase in yield (based upon I^2 scaling), but

not a flattening of the yield curve at large diameter. Thus, the higher yields for large diameter arrays in the present experiments must be due either to more wires (24 vs. 12) or more current return posts (12 vs. 6). As discussed below, we believe that improved current return symmetry provides the most likely explanation.

X-ray images of the imploded plasma were taken using a time-integrated pinhole camera filtered with 10-μm titanium. This filter has a transmission of only 0.1% for the Aℓ H-α line, so the images are indicative of higher spectral components; the characteristic transmission (37%) occurs at 3.5 keV. Figure 1-6 presents x-ray images for 6 typical loads with wire array diameters ranging from 15 to 32 mm. Note that the larger diameter arrays appear shorter because of the line-of-sight occlusion described above. More importantly, all the loads appear to have imploded stably to a source diameter of about 2 mm, regardless of the initial diameter of the load. The x-ray images tend to corroborate the observation that x-ray yield does not fall off rapidly at large diameter in the present experiments. Thus, large-diameter arrays appear more promising than previously believed, at least for low atomic number elements like aluminum.

Finally, the observed x-ray yields are not well correlated with the coupling of kinetic energy to the plasma. This conclusion is better illustrated in Figure 1-7, which presents the mean x-ray yields as a function of array diameter and mass. Two sets of curves are superimposed upon the data: contours of constant moment of inertia (mr^2) and contours of constant η (ratio of kinetic ion kinetic energy to K-shell ionization energy). For zero-dimensional implosions the constant mr^2 lines are also lines of constant implosion kinetic energy; calculated values are shown on the curves assuming a cutoff at 10% of the initial radius. The x-ray yields appear random rather than showing any systematic trends with kinetic energy, mass or η. The highest conversion efficiency for kinetic energy into K-shell x-rays is about 65%.

1.5 RETURN CURRENT SYMMETRY.

Mosher (Reference 5) has shown that poor symmetry in the magnetic field of the current return cage will cause the individual wires to implode at different times, which severely limits the compression and density in the imploded array. The uneven acceleration results from the fact that wires aligned with the return posts will experience higher magnetic fields than wires aligned with the magnetic minima midway between the posts. This model actually underestimates the asymmetry at early times because it assumes equal currents in all wires, which is true only if the wires are highly resistive (i.e., inductive effects are negligible).
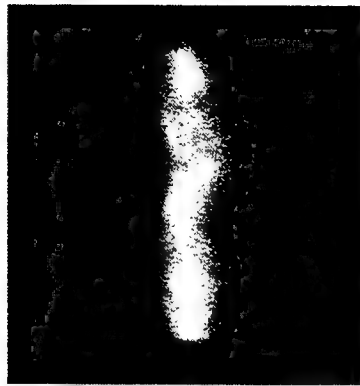
15-mm array diameter
12 wires; 277 µg/cm
shot 3160
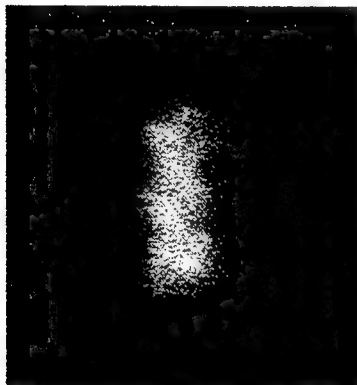
17.5-mm array diameter
12 wires; 369 µg/cm
shot 3172

22-mm array diameter
24 wires; 328 µg/cm
shot 3152
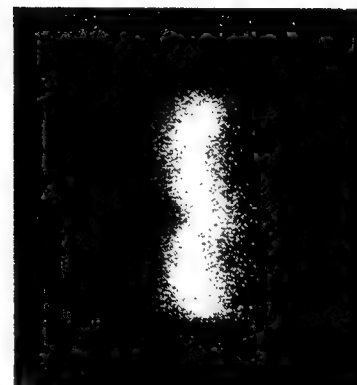
25.5-mm array diameter
18 wires; 246 µg/cm
shot 3142

27.5-mm array diameter
24 wires; 210 µg/cm
shot 3154
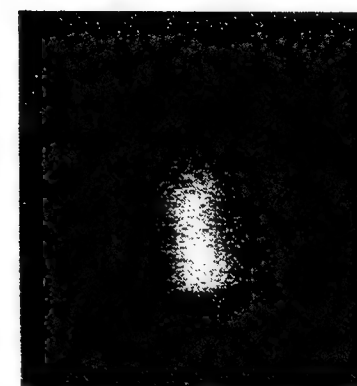
32-mm array diameter
24 wires; 161 µg/cm
shot 3144

Figure 1-6. Time-integrated x-ray images for wire array diameters from 15 to 32 mm.
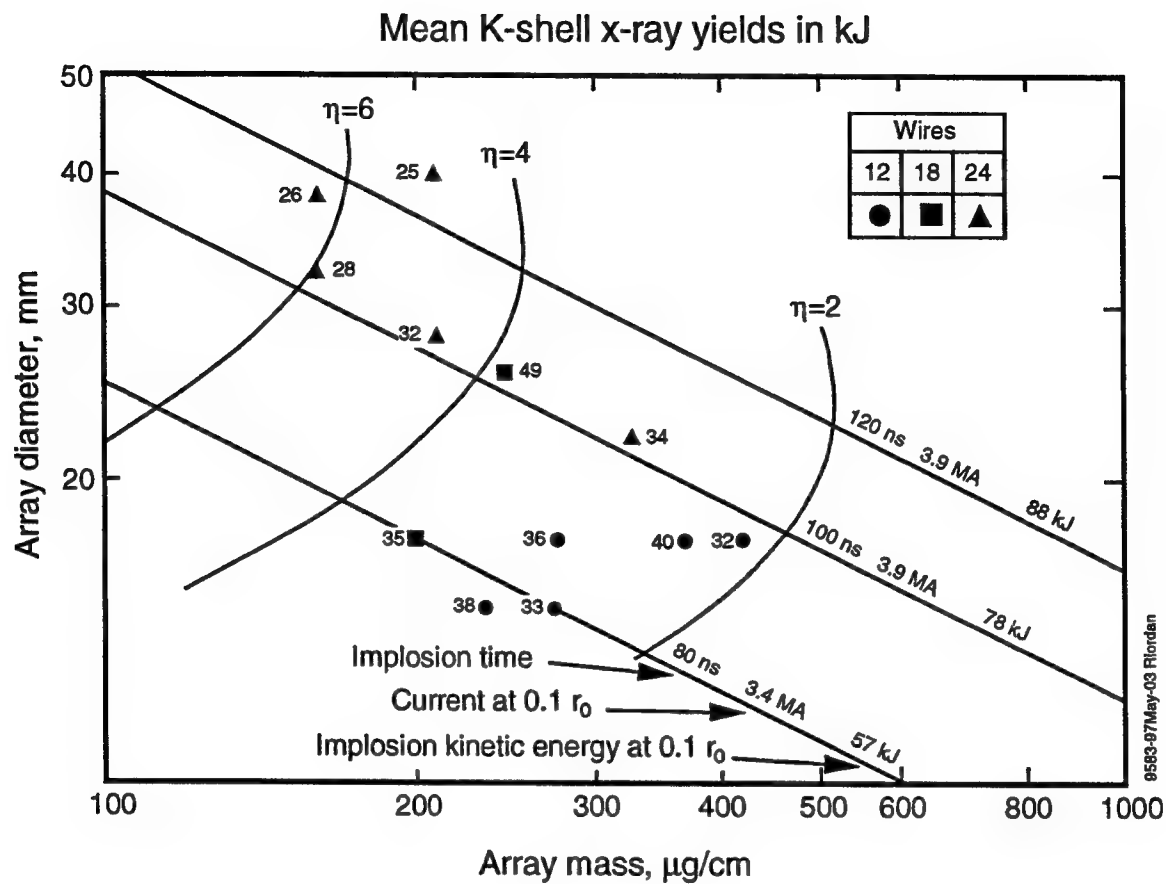
Figure 1-7. Mean aluminum K-shell yield (in kJ) versus array diameter and mass.

Following Mosher, we modeled the wires and current return posts as discrete elements and assumed that the currents were evenly divided between the individual wires. To quantify the asymmetry, we defined a ratio of the difference between the magnetic field maximum and minimum divided by the mean magnetic field. When all field quantities are evaluated on the initial circumference of the wire array, this asymmetry ratio is given by

$$\frac{\Delta H}{\langle H \rangle} = \frac{1 - \varepsilon^2}{2N} \sum_{n=1}^{2N} \frac{(-1)^n}{1 + \varepsilon^2 - 2\varepsilon \cos \frac{\pi n}{N}} , \quad \varepsilon = \frac{r_o}{R} ,$$

where N is the number of current return posts and ε is the ratio of array radii for the wires and current return posts. Figure 1-8 shows the calculated asymmetry ratios for return cages with six and twelve posts plotted as a function of the wire-to-return radius ratio. The dashed lines represent the minimum compression radii as calculated by Mosher.

As expected, the asymmetry and compression are much worse for the six-post return cage. The solid points represent the specific load hardware used in the experiments of 1989 (six posts) and the present study (twelve posts). Note that the 20-mm and 25-mm diameter arrays with six posts have 44% and 60% asymmetries, respectively, which can easily explain the low yields achieved with these loads. With twelve posts, on the other hand, the 25.5-mm load has only 4% asymmetry, and the worst asymmetry at 40-mm diameter is only 15%. We believe that improved current return symmetry is largely responsible for the improved yields with large diameters in the present experiments, but a controlled experiment is needed to confirm this hypothesis.

14
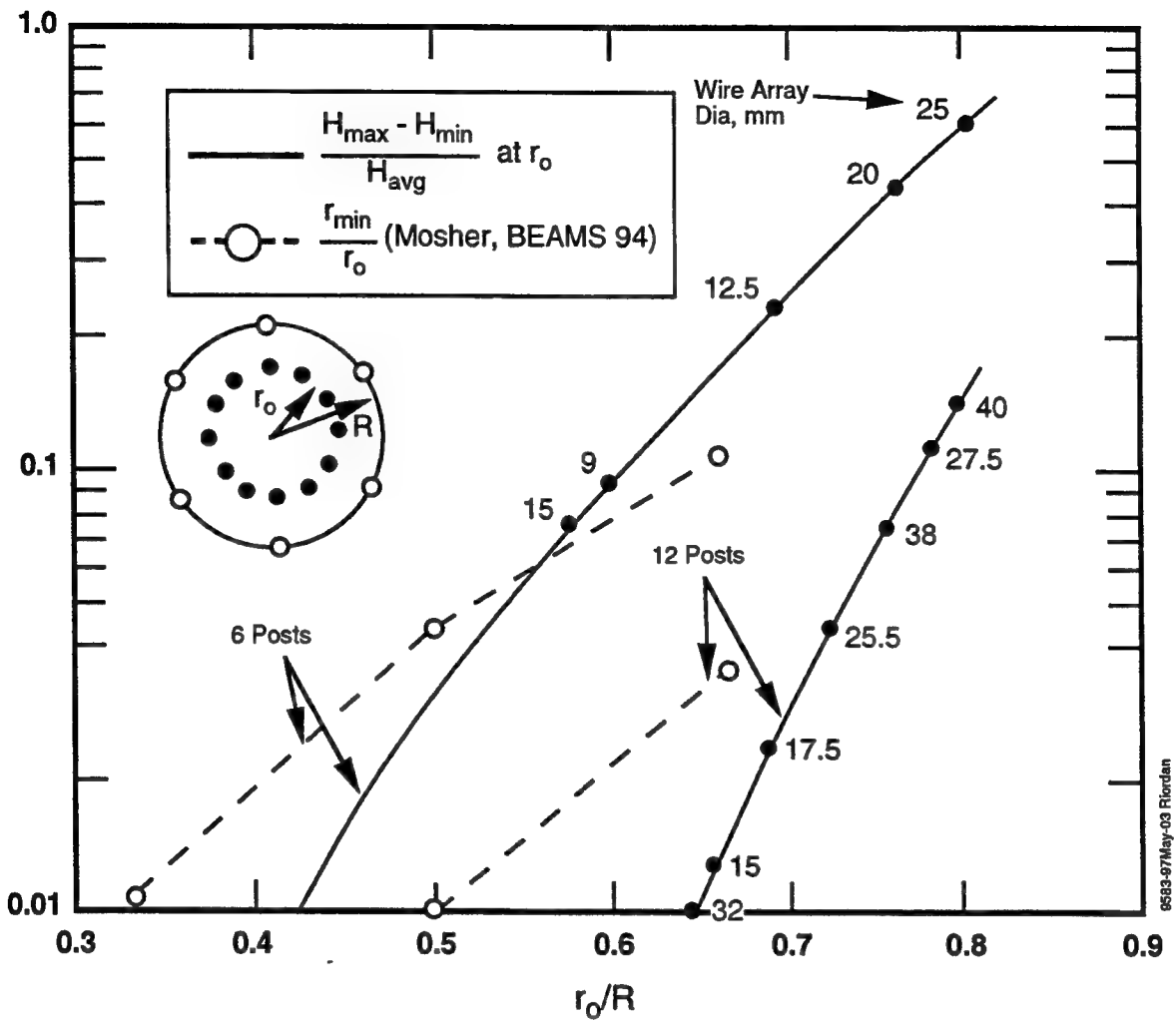
Figure 1-8. **Magnetic field asymmetry and minimum implosion radius as a function of the wire-to-return radius ratio.**

15

SECTION 2

ALUMINUM/MAGNESIUM WIRE ARRAYS

X-ray emission from plasma radiation sources of low atomic number (e.g., neon and aluminum) is limited by opacity in the He-like and H-like resonance lines. Apruzese and Davis (Reference 6) have calculated that the K-line x-ray power from optically thick plasmas could be nearly doubled by using a 50/50 mixture of elements of adjacent atomic number. Deeney et al (Reference 7) have already reported increased K-shell yields in earlier experiments using arrays of magnesium-coated aluminum wires.

The experiments described below provide a larger database that confirms a nearly 20% increase in x-ray yield for magnesium-coated aluminum wire loads compared to arrays of pure aluminum wires. Time-resolved spectroscopy, however, reveals that much of the increased yield is due to the complex dynamics of wire array implosions. It appears that the magnesium coating evaporates, slips between the remaining aluminum wire cores, and implodes earlier to produce a hot magnesium plasma that begins radiating 10-ns before the aluminum plasma. Additional experiments with alloy (rather than coated) wires and with 50% more wires lend support to this interpretation and also suggest the importance of compressive heating for increasing the x-ray yield.

2.1 WIRE ARRAY LOADS.

The primary objective of these experiments was to compare the x-ray performance of aluminum/magnesium mixtures to that of pure aluminum wire arrays. Thus, the wire array loads were designed to minimize the variation in other load parameters. In particular, all loads used 20-mm-long wires in a 15-mm-diameter array. Most of the load masses were held within a range of 263 to 308 μg/cm; some variation in load mass was unavoidable because the wires are available only in discrete sizes. The magnesium fraction was varied from zero to 60% by vacuum deposition of a 100% Mg coating onto a 100% Al core wire. In addition to the coated wires, several arrays of alloy wires were also tested to compare a magnesium coating to magnesium mixed uniformly in the wire.

All the loads were tested on the Double-EAGLE generator operated with the Marx bank charged to 60 kV. The experiments were actually performed in two separate sessions; the preliminary tests occurred in 1993 (shots 28xx in the tables below) and the confirmation tests occurred 1994 (shots 3xxx). During the 1993 tests the magnesium coating tended to oxidize during storage and to delaminate during assembly of the wires into the array. For the 1994 tests, we ordered a new

set of wires and attempted to mitigate the oxidation by storing them in dry air. The current return cage also differed for the two test sessions; the 1994 tests used the new 12-post cage described in Section 1.1, while the 1993 tests used the old 6-post cage. Nevertheless, we do not expect significant differences because of the minimal return cage asymmetry for both cases (1% and 8% respectively).

2.2 X-RAY MEASUREMENTS.

The K-shell x-ray yields were measured using a pair of filtered calorimeters and a pair of filtered PCDs as described in Section 1.3. Because the spectrum varied depending upon the magnesium content, however, we did not use a constant factor to correct for filter transmission. Instead, we calculated the filter transmission using measured x-ray spectra from a number of typical shots with various magnesium fractions. For the remaining shots the filter transmission was estimated, i.e., interpolated based upon the magnesium fraction of the load.

Table 2-1 summarizes the data for the magnesium-coated aluminum wire arrays grouped in order of increasing magnesium fraction. The NS timing column is the difference in arrival times for the north and south pulses on Double-EAGLE; absolute timing differences greater than 20 ns are often associated with low currents and low yields. The implosion time is defined as in Section 1.2. Yield measurements are presented here only for calorimeter #1, which was fielded on all shots; the other three yield diagnostics were not functioning properly during the 1993 experiments. The mean and standard deviation for the yield measurements of similar loads are presented below each group. The yield shows an apparent peak of 38.5 kJ at 20% Mg, but the standard deviation is rather large (Figure 2-1a). The peak may be broader than it appears, because poor synchronization (>30 ns timing difference) reduced the yield for most the 10% Mg shots.

In an attempt to reduce the scatter in the yield data, we have further restricted the data to 12-wire arrays from 1994 to eliminate the variation caused by delamination and variation in wire number. These shots generally had four yield diagnostics, which also helped to reduce statistical noise. Indeed, Table 2-2 shows the standard deviations in yield are reduced by nearly a factor of 2. A plot of the restricted data (Figure 2-1b) shows that the yield peak at 20% Mg is now more than a standard deviation above the 0% and 30% Mg yields.

17

Table 2-1. Summary of experimental data for magnesium-coated aluminum wire arrays of similar mass.

Shot No.	Mg Fraction (%)	Wire No.	Al Diam. (mil)	Wire Mass (µg/cm)	NS Timing (ns)	Implosion Time (ns)	Peak Current (MA)	XRD FWHM (ns)	Cal 1 Yield (kJ)
2802	0	14	1.2	276	-21	87	3.7	23	36.4
3149	0	12	1.3	277	24	86	3.9	26	24.5
3150	0	12	1.3	277	-24	82	3.7	33	24.9
3159	0	12	1.3	277	9	80	4.3	26	29.3
3160	0	12	1.3	277	-16	80	3.7	20	31.5
3161	0	12	1.3	277	0	-	-	36	37.8
3162	0	12	1.3	277	-8	-	3.8	-	31.5
Mean									32.3
St. Dev.									4.6
2811	10	12	1.2	263	-9	75	-	28	35.0
2812	10	12	1.2	263	-33	95	-	33	31.4
2813	10	12	1.2	263	-32	92	-	27	32.6
2844	10	12	1.2	263	-36	96	-	31	32.8
Mean									33.0
St. Dev.									1.5
2814	20	12	1.2	295	-14	93	-	35	46.3
2815	20	12	1.2	295	14	87	-	25	57.5
2843	20	12	1.2	295	-18	85	-	33	35.5
3074	20	12	1.2	295	-20	80	4.0	46	42.2
3075	20	12	1.2	295	-12	80	3.9	30	34.7
3080	20	12	1.2	295	10	89	3.6	30	43.4
3083	20	12	1.2	295	-1	83	4.0	30	2.91
3077	20	18	1.0	308	7	100	4.0	30	22.6
3078	20	18	1.0	308	7	91	3.9	20	34.7
Mean									38.5
St. Dev.									10.3
3085	30	12	1.1	284	7	85	4.0	35	27.6
3086	30	12	1.1	284	-11	85	3.9	27	28.6
Mean									28.1
St. Dev.									0.7
2836	50	16	0.8	280	-14	-	-	16	35.3
2841	50	16	0.8	280	8	100	-	31	28.8
2845	50	16	0.8	280	8	93	-	22	43.7
Mean									35.4
St. Dev.									7.5
2839	60	12	0.8	263	7	87	-	25	36.6
2842	60	12	0.8	263	19	90	-	22	26.2
Mean									31.4
St. Dev.									7.4
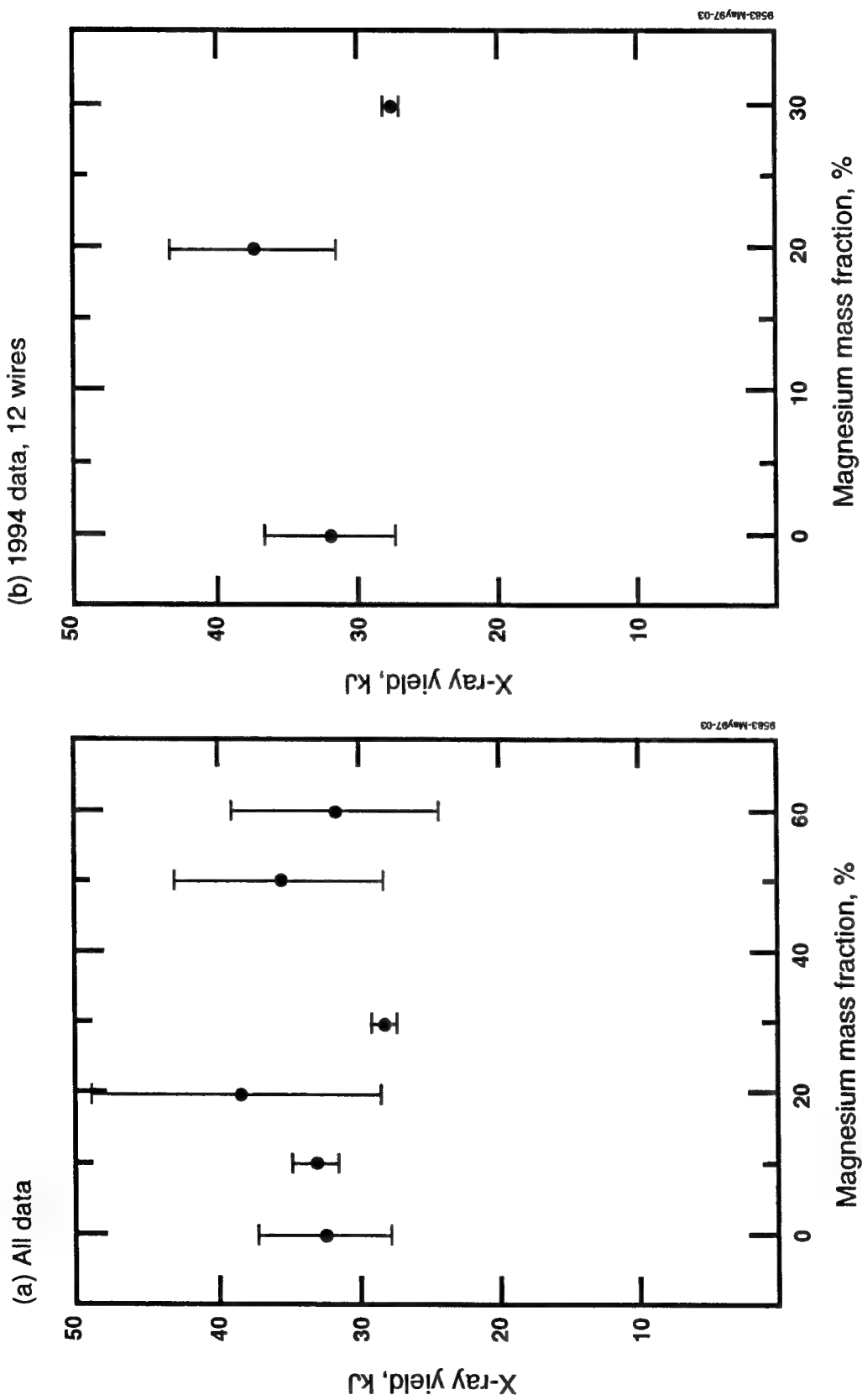
Figure 2-1. Mean and standard deviation of K-shell x-ray yields versus magnesium mass fraction for array with masses between 263 and 308 mg/cm; (a) calorimeter #1 data for all arrays; b) calorimeter #1 data for 12-wire arrays from the 1994 experiments.

Table 2-2. Summary of experimental data for 12-wire and 18-wire arrays.

Shot No.	Wire No.	Mg Fraction (%)	Al Diam. (mil)	Wire Mass (μg/cm)	Cal 1 Yield (kJ)	Cal 2 Yield (kJ)	PCD8 Yield (kJ)	PCD9 Yield (kJ)	Avg. Yield (kJ)	XRD FWHM (ns)	PCD FWHM (ns)
3149	12	0	1.3	277	24.7	-	31.7	30.1	-	26	32
3150	12	0	1.3	277	35.2	-	38.9	38.2	-	32	46
3159	12	0	1.3	277	29.5	26.6	31.3	29.8	29.3	26	32
3160	12	0	1.3	277	31.7	28.6	37.5	35.9	33.4	20	24
3161	12	0	1.3	277	38.1	32.4	37.5	35.3	35.8	36	40
3162	12	0	1.3	277	31.7	30.5	-	-	-	-	-
Mean					31.8	29.5	35.4	33.9	32.8	28.0	34.8
St. Dev.					4.6	2.5	3.6	3.7	3.3	6.2	8.4
3074	12	20	1.2	295	42.2	39.6	41.7	42.6	43.0	46	46
3075	12	20	1.2	295	34.5	34.5	37.9	36.4	36.7	30	32
3080	12	20	1.2	295	43.6	42.3	45.0	42.4	42.7	30	30
3083	12	20	1.2	295	28.9	23.4	33.2	30.2	30.4	30	30
Mean					37.3	35.0	39.5	37.9	38.2	34.0	34.5
St. Dev.					6.0	7.2	4.4	5.1	5.2	8.0	7.7
3085	12	30	1.1	284	27.6	27.6	35.5	32.8	30.9	35	38
3086	12	30	1.1	284	28.0	24.8	35.5	33.5	30.5	27	29
Mean					27.3	26.2	35.5	33.2	30.7	31	33.5
St. Dev.					0.3	2.0	0.0	0.5	0.3	5.7	6.4
3077	18	20	1.0	308	22.6	22.6	30.2	28.4	26.0	30	30
3078	18	20	1.0	308	34.7	30.7	36.2	34.4	34.0	20	24
Mean					28.7	26.7	33.2	31.4	30.0	25.0	27.0
St. Dev.					8.6	5.7	4.2	4.2	6.3	7.1	4.2

2.3 STATISTICAL ANALYSIS.

There has been some controversy as to whether the increased yield with 20% Mg is real or merely a statistical fluctuation. Thus, we have used a standard statistical technique to assess the validity of the effect. Suppose we have two samples with n_1 and n_2 data points, which have respective means y_1 and y_2, and sample standard deviations s_1 and s_2. We need to determine whether the two samples are just statistical fluctuations within the same population or are really samples from two different populations. The "t-test" compares the difference between the two means to a "pooled" standard deviation, s, defined by

$$s^2 = \frac{\left(n_1 - 1\right) s_1^2 + \left(n_2 - 1\right) s_2^2}{n}$$

where $n = n_1 + n_2 - 2$ is the degrees of freedom. The quantity t is the difference in means divided by the expected deviation in the mean

$$t = \frac{y_2 - y_1}{\sqrt{s^2\left(\dfrac{1}{n_1} + \dfrac{1}{n_2}\right)}} \ .$$

One then uses a t-distribution probability table to find $P(t>t_o;n)$, the probability that the t would be at least as large as the observed value t_o if the two samples actually came from the same population.

We now apply the t-test to compare the difference in yields for 20% Mg and 0% Mg for three different classes of yield data, as shown in Table 2-3. Using only calorimeter #1 with no restrictions on wire number, we find t=1.47 (the difference in means is 1.47 times the expected standard deviation) and the probability of such a large fluctuation is only 9%. In other words, we have 91% confidence that the observed yield increase is a real effect of the difference in wire composition. If we restrict the data to 12-wire arrays, the confidence level improves to 93% using only the #1 calorimeter data. Using the average yield from all four diagnostics, the confidence level decreases slightly to 91% because we had to ignore 3 shots with incomplete data.

Table 2-3. Statistical analysis of K-shell yields.

Data Set	0% Mg			20% Mg			Pooled			$P(\geq t_o;n)$	Confidence Level
	n_1	y_1	s_1	n_2	y_2	s_2	n	s^2	t_o		
Cal#1 all wires	7	32.3	4.6	9	38.5	10.3	14	69.7	1.47	9%	91%
Cal#1 12 wires	6	31.8	4.6	4	37.3	6.0	8	26.7	1.65	7%	93%
4 Diagnostics 12 wires	3	32.8	3.3	4	38.2	5.2	5	20.6	1.63	9%	91%

Thus we are highly confident that the 20% Mg mixture produces a higher K-shell yield (about 38 kJ) than a pure aluminum array (about 32 kJ). The magnitude of this increase (nearly 20%) is consistent with the 20% increase predicted upon the basis of reduced K-line opacity effects for an electron temperature near 600 eV as shown in Figure 2-2. Nevertheless, time-resolved spectral measurements described below suggest that early implosion of the magnesium coating also plays an important role in the radiation output of mixed element loads.
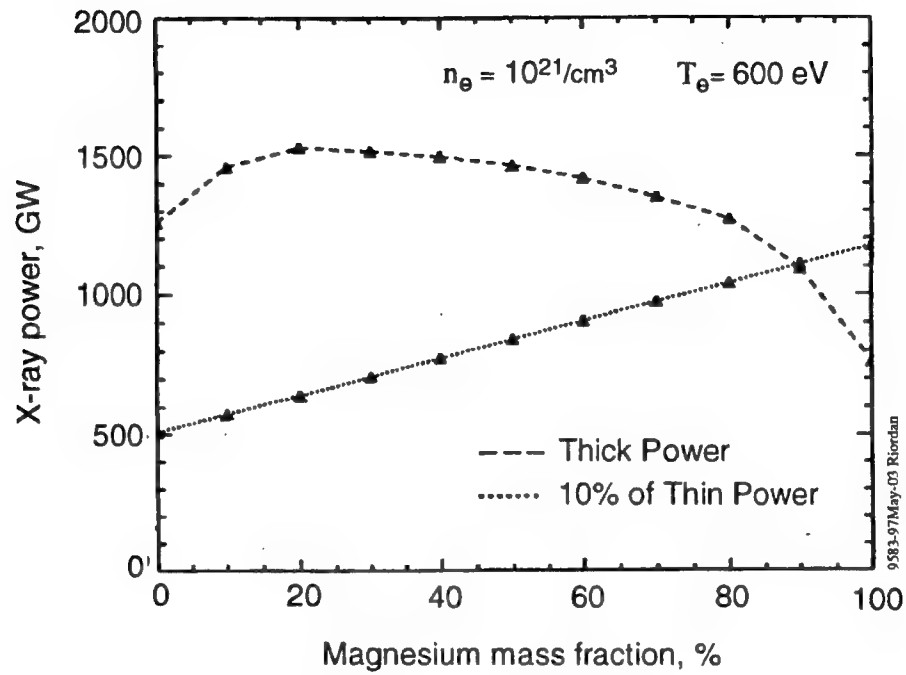
Figure 2-2. Predicted K-line x-ray power for a 3-mm diameter aluminum/magnesium plasma at a temperature of 600 eV and a density of 10^{21} electrons/cm^3 (Reference 6).

2.4 WIRE PLASMA INITIATION.

Our present understanding of aluminum wire arrays as plasma radiation sources is based upon the assumption that the individual wire plasmas merge at a very early time into a cylindrical plasma shell, which then undergoes a one-dimensional implosion (Reference 1). Recent experiments, however, have shown that the number of wires (or the gap between wires) has a significant effect upon the x-ray yield and pulse width, even for arrays with the same mass. Because the magnesium coating and the aluminum core radiate at different photon energies, the coated wire array provides a serendipitous probe of the evolution of the individual wire plasmas.

The first evidence for non-cylindrical implosion of the wire plasmas was provided by the time-gated spectrometer, which images the H-α and He-α lines of both magnesium and aluminum. Figure 2-3a shows a spectrum taken for a typical 12-wire array with 20% Mg as a coating; the frames are separated by 10 ns and each frame is gated on for 5 ns. The magnesium Mg H-α line is clearly evident in the first frame, but the aluminum lines are not observed until 10 ns later. The lack of a strong Mg He-a line indicates that the magnesium temperature is >1 keV, high enough that any aluminum in the same region would also be radiating efficiently. Thus we conclude that the magnesium has separated from the aluminum, i.e., the magnesium coating has evaporated first and imploded onto the array axis before the arrival of the aluminum plasma from the wire core.

To provide additional data for this interpretation, we also tested arrays of 12 wires fabricated from aluminum alloys containing 6% Mg and 1% Mg ; data are summarized in Table 2-4. Time-gated spectra for the 6% Mg alloy (Figure 2-3b) show that the magnesium and aluminum lines turn on simultaneously for alloy wires, indicating that both elements are well mixed in the radiating plasma. Comparing the relative intensities of the H-α and He-α lines in the time-integrated spectra (Figure 2-4), we also conclude that the magnesium and aluminum have about the same temperature for the alloy wires, but the aluminum plasma is significantly colder for coated wires. These results are perfectly understandable, given that the two elements are well mixed at the surface of the alloy wires, but not at the surface of the coated wires.

Table 2-4. Summary of experimental data for Mg/Al alloy loads.

Mg Fraction (%)	Wire No.	Wire Diam. (mil)	Wire Mass (μg/cm)	Implos. Time (ns)	Peak Current (MA)	Cal Yield (kJ)	PCD Yield (kJ)	XRD FWHM (ns)	PCD FWHM (ns)
0	12	1.2	236	-	-	38.6	44.7	34	30
1	12	1.2	236	84	3.9	37.8	39.1	37	-
1	12	1.2	236	-	-	31.2	31.1	23	-
6	12	1.2	231	80	4.0	40.3	38.8	40	26
6	12	1.2	231	75	3.7	34.4	39.3	40	32
6	12	1.2	231	85	3.8	39.5	42.8	29	26

(a) 20% Mg as coating

t_o
$t_o + 10$ ns
$t_o + 20$ ns
$t_o + 30$ ns
$t_o + 40$ ns

Al
H-α

Al
He-α

Mg
H-α

Mg
He-α

(b) 6% Mg as alloy

t_o
$t_o + 10$ ns
$t_o + 20$ ns
$t_o + 30$ ns
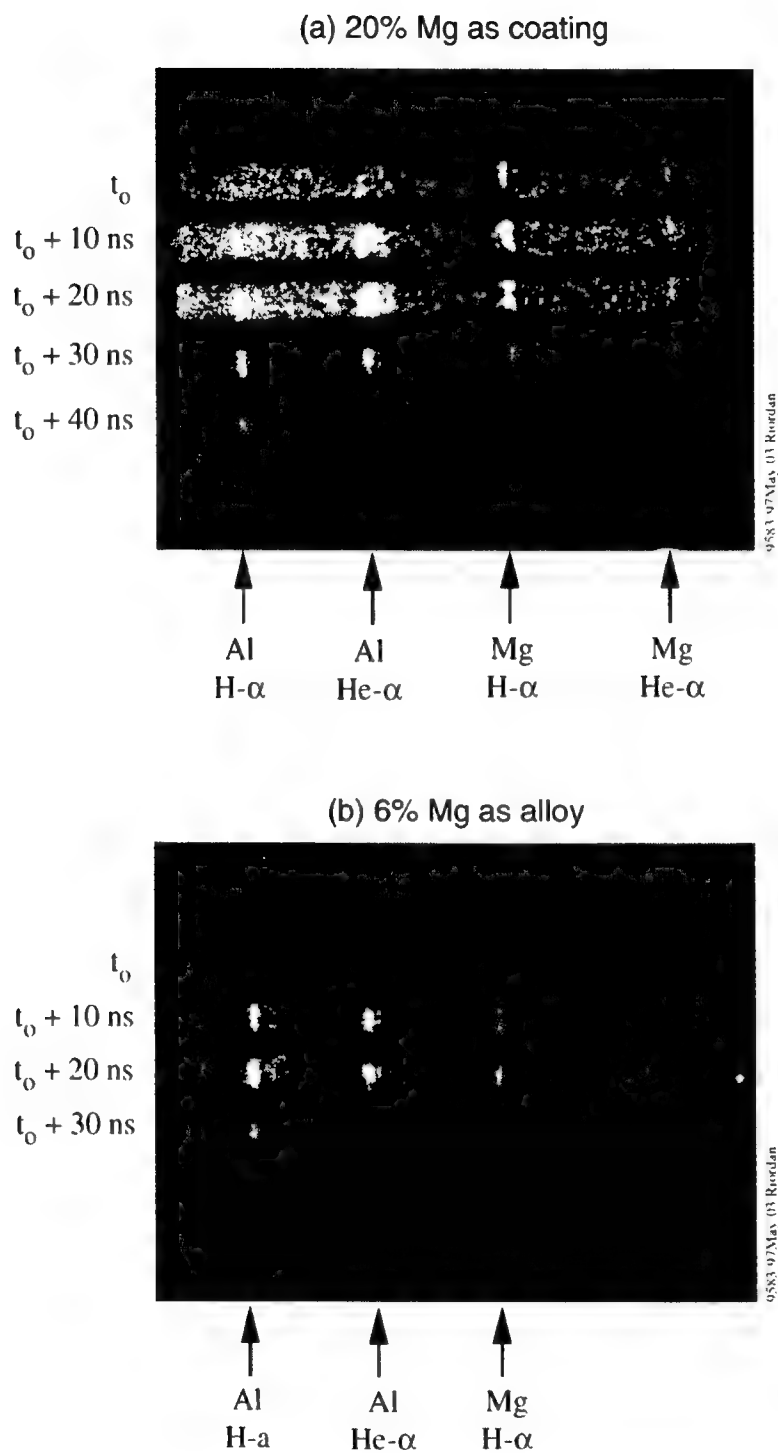
Al
H-a

Al
He-α

Mg
H-α

Figure 2-3. Comparison of time-gated K-line spectra for 12-wire arrays;
(a) 20% Mg as a coating (shot 2814); (b) 6% Mg alloy (shot 3076).
All frames are 5 ns in duration.

24
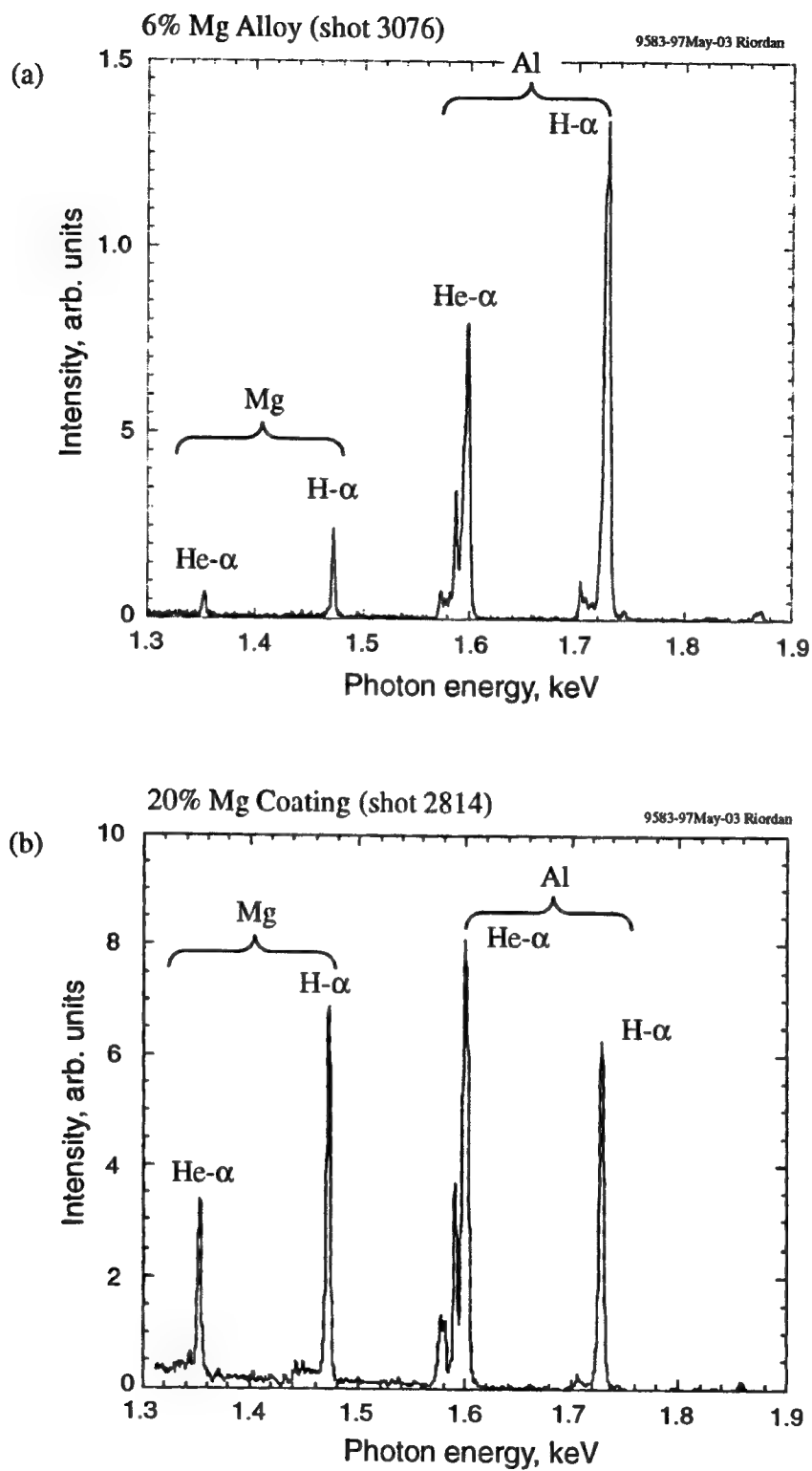
Figure 2-4. Comparison of time-integrated K-line spectra for 12-wire arrays; (a) 6% Mg alloy (shot 3076); (b) 20% Mg as a coating (shot 2814).

Further insight can be gained by increasing the number of wires in the array from 12 to 18, thereby decreasing the gap between adjacent wires. The time-gated spectra for the 18-wire loads (Figure 2-5a) show that the Mg lines are weaker and do not turn on early. The most probable explanation is that the wire plasmas have merged into a cylindrical shell very early in the implosion (Figure 2-5b). Closure of the gaps between the individual wires would inhibit magnetic field penetration inside the array and thereby prevent the acceleration of the coating plasma toward the axis. Additional confirmation for this hypothesis is provided by the x-ray pulse widths (FWHM), which are on average 8 to 9 ns longer for 12-wire loads than for 18-wire loads (see Table 2-2). As long as plasma is able to stream through the inter-wire gaps and entrain current, less current flows in the core wires, thereby reducing their acceleration. Early implosion of the coating and later implosion of the core both tend to produce a broader x-ray pulse.

Conventional wisdom predicts that the 18-wire loads should have produced higher yields than the 12-wire loads because of the improved cylindrical symmetry. The experimental data, however, show the opposite result. Although the number of shots is small, the data of at the bottom Table 2-2 show that the 18-wire array yields were lower by more than a standard deviation compared to 12-wire arrays with the same mass and magnesium fraction. One hypothesis for the increased yield and pulse width of the 12-wire loads is compression of the axial magnesium plasma by the aluminum plasma that implodes later. Compressive heating will couple additional energy to the plasma that can be radiated as x-rays. This additional energy may also explain the fact that the measured aluminum x-ray yields are often a factor often a factor of two or three higher than the theoretical predictions.

(a)   18 wires, 20% Mg coating

t_o
$t_o + 10$ ns
$t_o + 20$ ns
$t_o + 30$ ns

Al   Al   Mg
H-a   He-a   H-α

(b)

12 Wires   18 Wires
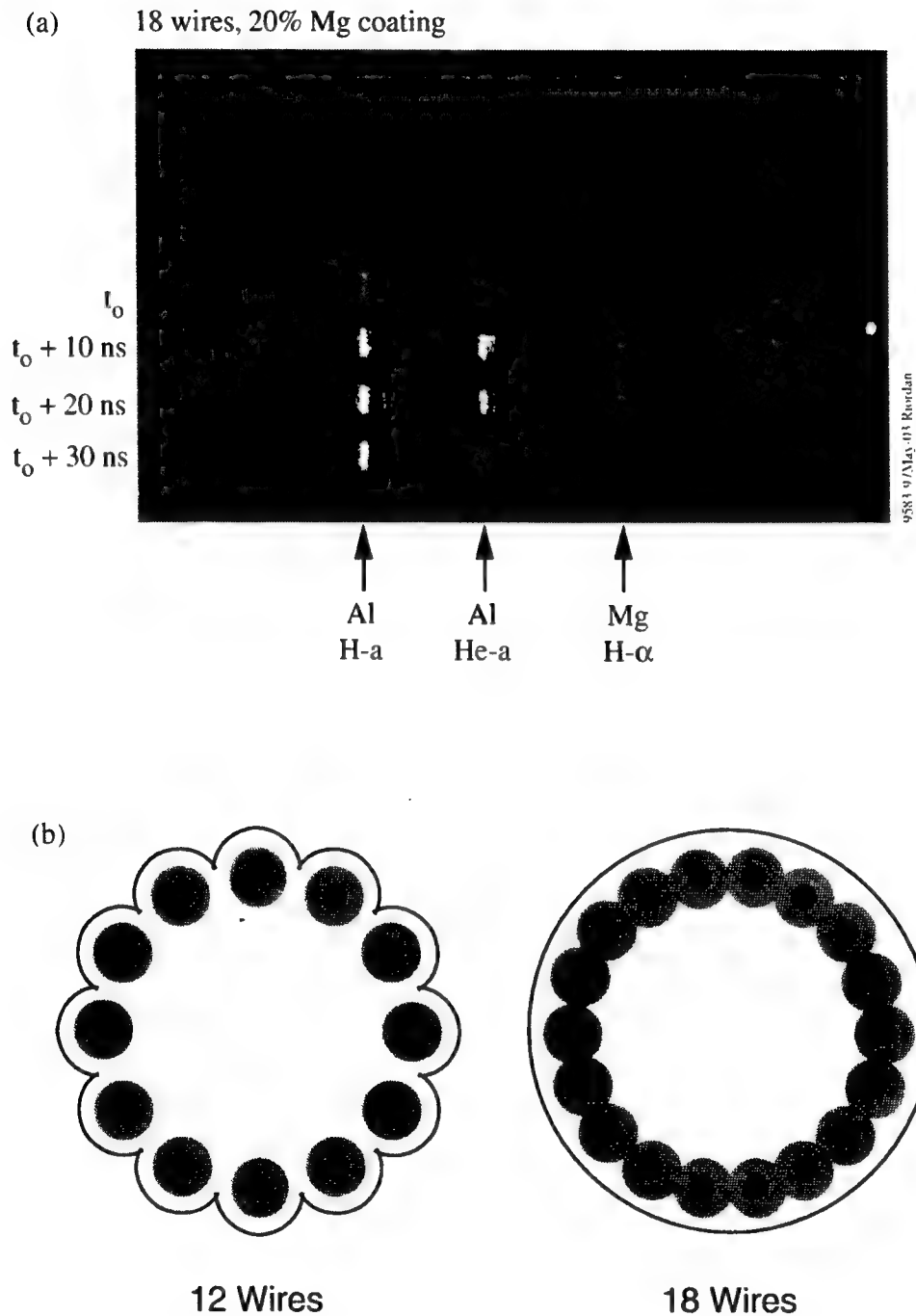
Figure 2-5.   Effect of increasing wire number; (a) time-gated K-line spectrum for an
18-wire array with 20% Mg as a coating (shot 3078); (b) merging of wire
plasmas into a cylindrical shell.

27

SECTION 3

ARGON/TITANIUM PUFF ON WIRE

Recent upgrades to the Double-EAGLE simulator (funded under a separate program) have improved the spectral fidelity of the 3.1-keV argon PRS by adding a small fraction of krypton, which is an intense L-shell radiator at 1.6 to 2.0 keV. This mixed-element PRS radiates a broadband x-ray spectrum that provides a better simulation of dose-depth profiles from a 1-keV blackbody threat. To provide a high-fidelity simulation including the high-energy tail, we need to add a third spectral component at approximately 5 keV.

A theoretical investigation by Thornhill (Reference 8) showed that a titanium wire on the axis of an annular argon gas puff could produce a mixed-element PRS that would be an efficient radiator of >4.7-keV x-rays. The wire provides the high-density core plasma that is required for efficient radiation, particularly for higher-atomic number elements (such as titanium) whose kinetic energy is only marginally sufficient for ionization into the K-shell.

The experiments described below did indeed ionize the titanium wire into the K-shell. Nevertheless, the best shots produced only about 1 kJ of titanium K-shell x-rays, and the core densities were significantly lower than expected. Diffusion or turbulent mixing of the titanium and argon plasmas may explain the discrepancy between theory and experiment.

3.1 PUFF-ON-WIRE LOADS.

The puff-on-wire load configuration consists of a single titanium wire on the axis of an annular gas puff, as illustrated in Figure 3-1. For these experiments we used 20- and 25-μm diameter wires of 100% titanium to produce a mass fraction on the order of 10% titanium in the combined load. The wire was vertically suspended from the center stub of the nozzle using a small bead of epoxy; a piece of copper tape attached to the bottom end of the wire provided tension to keep the wire straight.

The argon gas jet was produced using our standard 25-mm diameter annular nozzle with a nominal 5-mm exit width and a 10-degree inward tilt angle. We used nominally 100% argon for all of the shots except two, which used a gas mixture containing 5% krypton (partial pressure). The 37-mm plasma length was set by a radial wire mesh located 37 mm downstream from the nozzle exit.

All these experiments were performed on the Double-EAGLE generator operated with the Marx bank charged to 60 kV. Under these conditions, Double-EAGLE delivers a peak current of 3.0 to
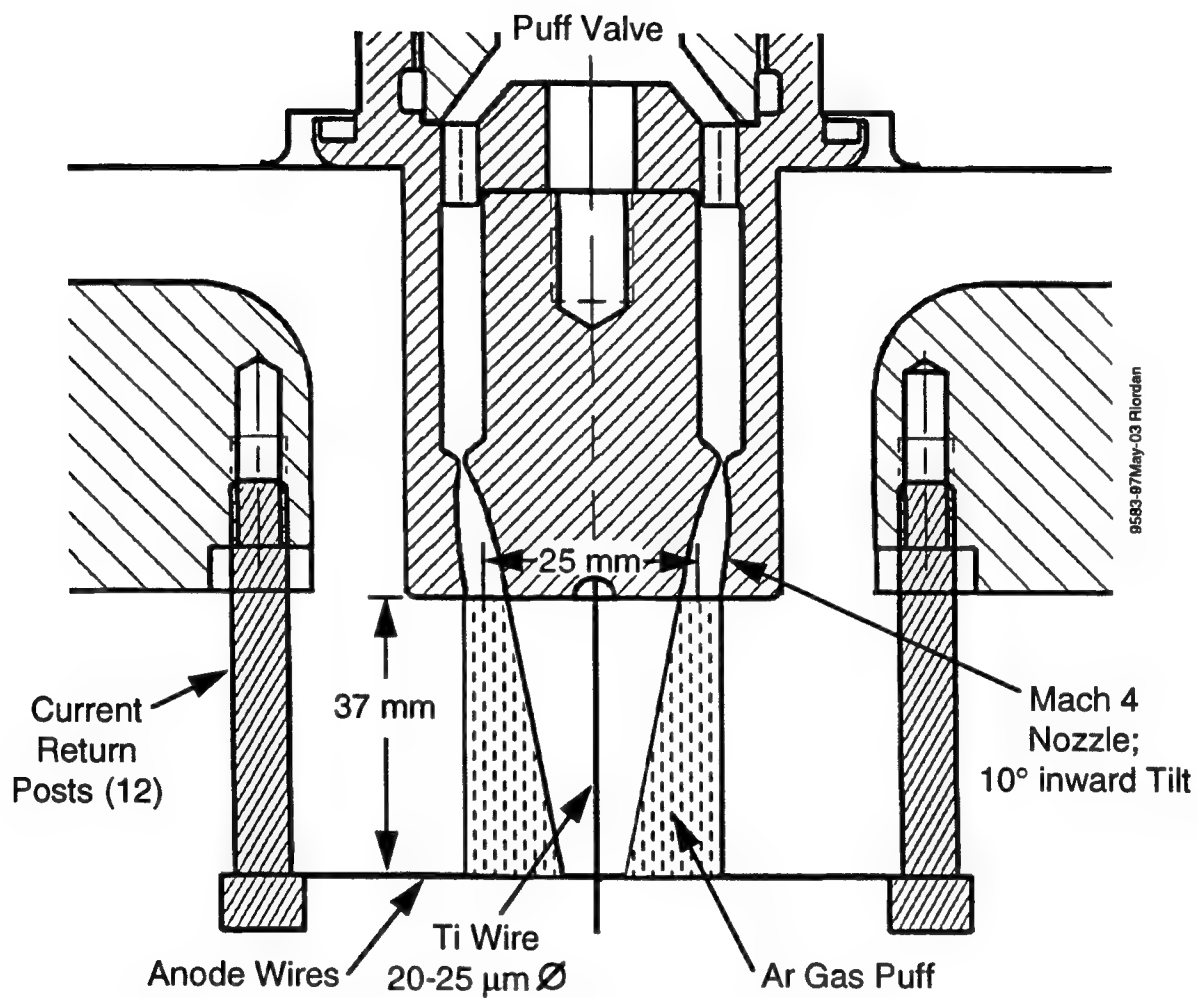
Figure 3-1. Puff-on-wire load configuration.

3.5 MA to an argon gas puff load, which is significantly lower than the peak current delivered to the wire array loads. The reduced current results from the increased inductance of the gas puff load, whose length and return cage diameter are about twice those of a wire load. Figure 3-2 shows typical load current and x-ray power waveforms.

3.2   X-RAY MEASUREMENTS.

The x-ray yields were measured using filtered calorimeters, filtered PCDs, and a time-integrated spectrometer as discussed in Section 1.3. To accommodate the complex, mixed-element spectrum, we made a number of modifications to the diagnostics. The spectrometer was modified to use two different curved crystals, PET and LiF, which provide good dispersion for the argon and titanium K-shell spectra respectively. Also, three of the PCDs were differentially filtered to provide narrow-band measurements of the titanium x-ray yield and power.

The measured x-ray spectra of Figure 3-3 show that the puff-on-wire load configuration ionizes both argon and titanium into the K-shell. The argon is predominantly He-like with a significant H-like fraction, similar to the 100% argon loads. Titanium, which has a higher ionization energy, is predominantly Li-like and He-like, with minimal H-like fraction. These spectra indicate that the argon and titanium plasmas are well mixed and have an electron temperature of about 1.8 keV, as discussed below.

Most of the titanium K-shell yield is radiated by a trio of 1s-2p transitions near 4.7 keV, which can easily be measured using a Ross pair of PCDs differentially filtered with scandium and titanium. Figure 3-4 shows transmission curves for the 25-μm scandium and 15-μm titanium filters, each of which is combined with an additional 25.4-μm Kapton filter. The difference of the two transmission curves provides a narrow pass-band between the K-edges at 4.5 and 5.0 keV. Although this filter arrangement will respond to argon recombination radiation in the pass-band, it provides excellent rejection of the argon K-lines below 4.5 keV. The transmission varies somewhat over the pass-band, but we have used the 47% differential transmission at 4.75 keV (the dominant line) in unfolding the yields.

We have also used a third PCD filtered with 10.8-μm aluminum and 25.5-μm Kapton to measure the x-ray yield above 5 keV. Although not strictly a Ross pair, the differential use of this filter with the Ti/Kapton filter will reject x-rays below 5 keV. In unfolding the yield above 5 keV we have used the 60% differential transmission at the mean line energy of 5.6 keV. This estimate may overestimate the >5-keV yield by up to 50%, depending upon the recombination continuum.
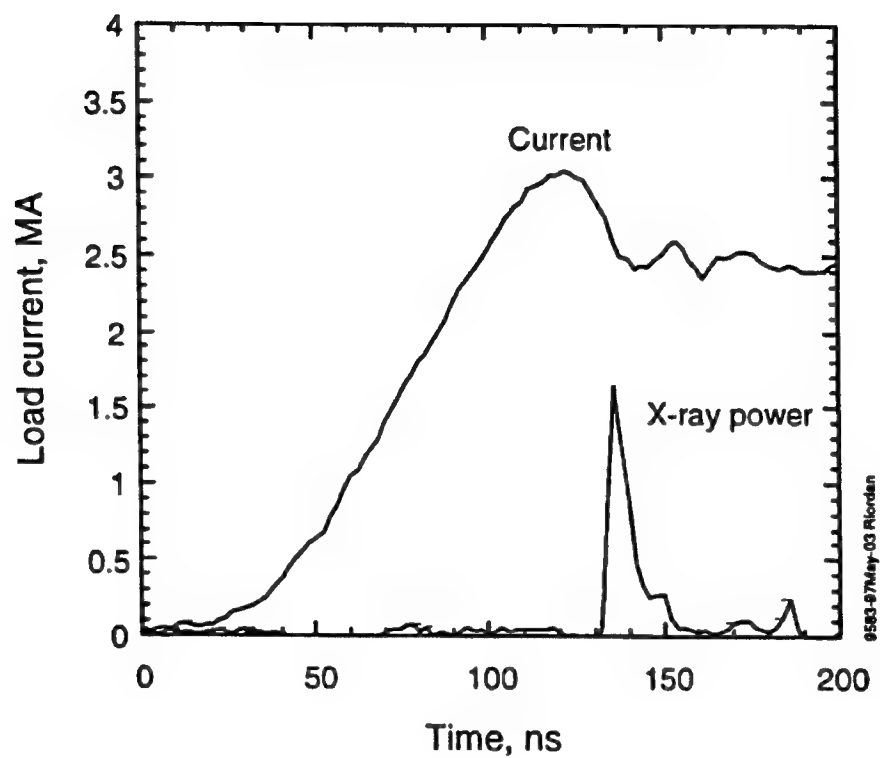
Figure 3-2. Typical load current and x-ray power waveforms.

(a)

He-α

Ar Spectrum

H-α

He-β

He-γ H-β

Ti

9583-97May-03 Riordan

Photon energy, keV

(b)

He-α

He
IC

Ti Spectrum

Li

He-β

Li

H-α

Li He-γ

9583-97May-03 Riordan

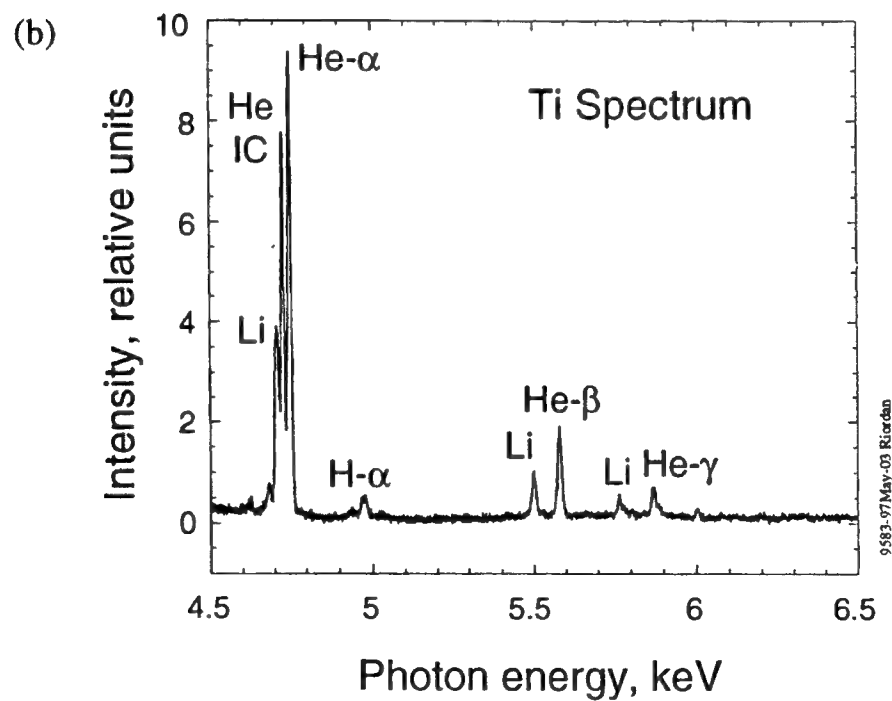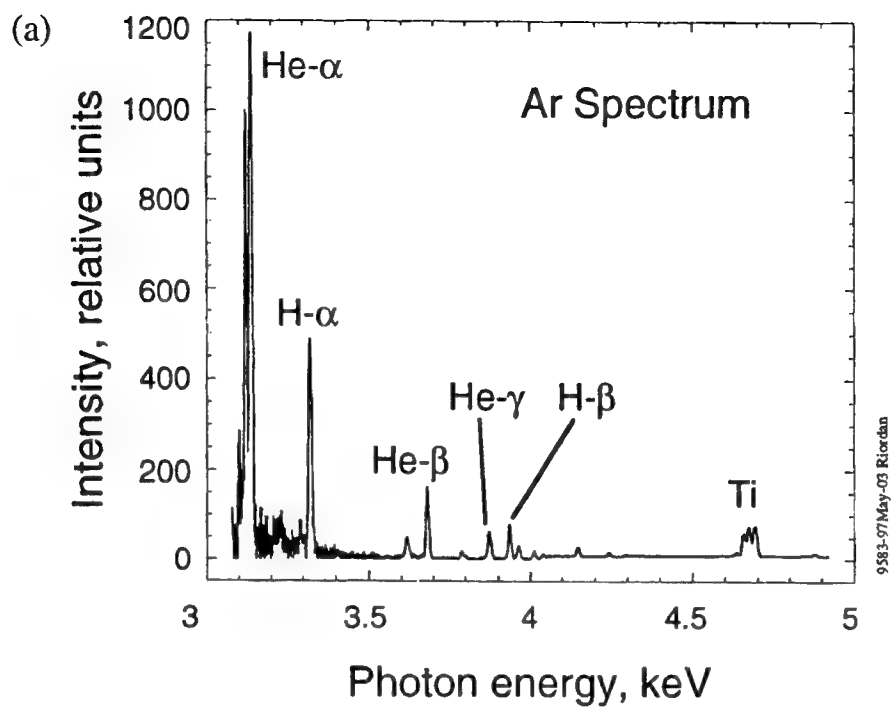Photon energy, keV

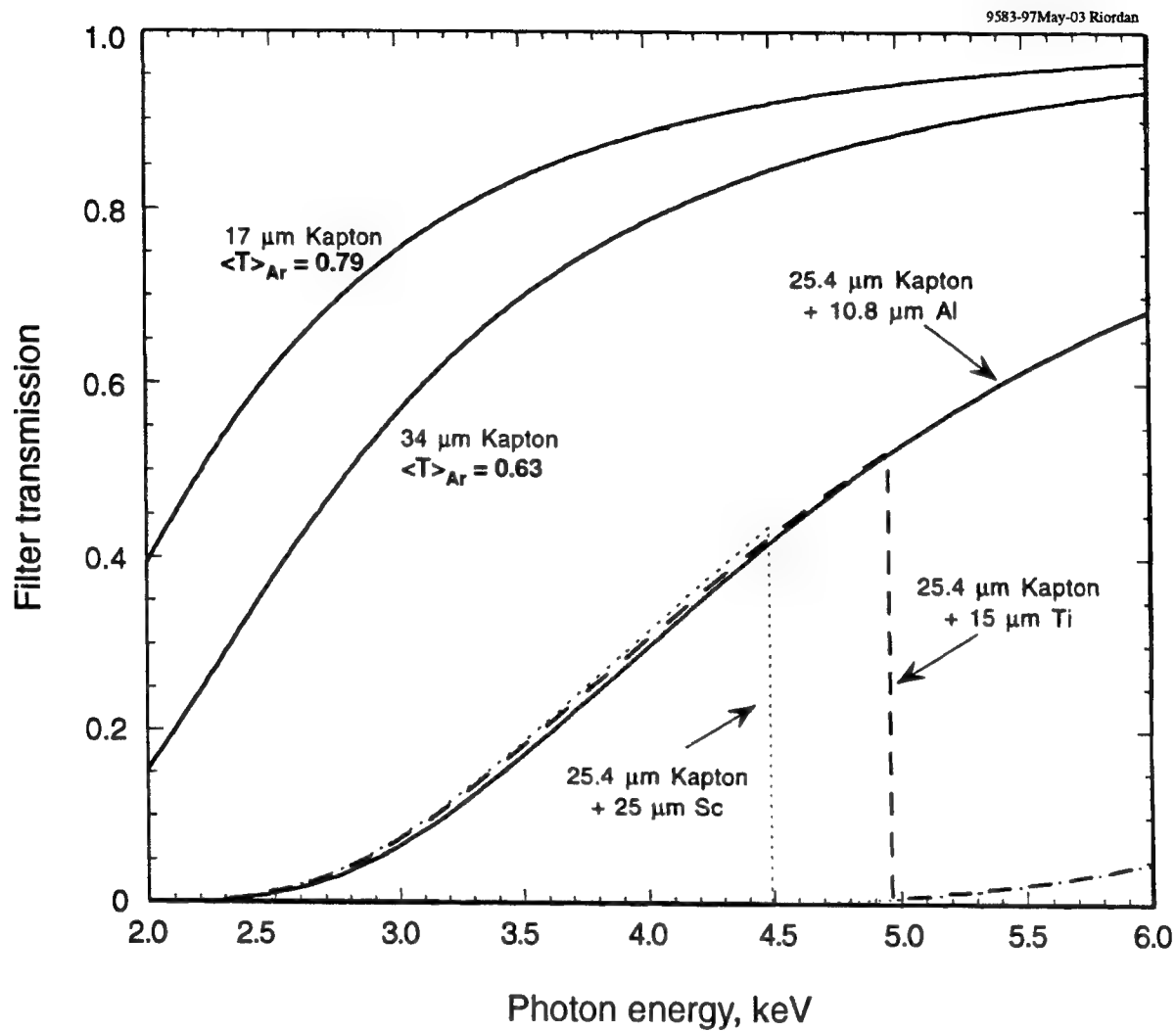**Fiure 3-3. Measured K-shell x-ray spectra; (a) argon and (b) titanium.**

Figure 3-4. **Calculated x-ray transmission curves for Ross pair filters and calorimeter filters.**

The yield above 3 keV is predominantly due to argon K-line radiation, which was measured using three tantalum calorimeters filtered to suppress the sub-keV radiation. Figure 3-4 shows transmission curves for the calorimeter filters of 17 and 34 μm Kapton. In unfolding the calorimeter yield measurements, we did not use a mean spectral energy as for the titanium. Rather, we used a spectrally-weighted transmission value calculated from a typical measured argon spectrum; the argon-weighted transmission values <T> are shown in Figure 3-4. For simplicity we have omitted the titanium lines from the spectral weighting; the error introduced by this omission is negligible (<2%) because the titanium yields are small and the argon-weighted filter transmission is high.

Figure 3-5 shows typical waveforms for x-ray power in the titanium (4.5 to 5.0 keV) and the argon (>3-keV) spectral ranges. The x-ray power in the titanium range has a 3-ns FWHM, half that of the argon range. The peak power in the titanium range, however, is a factor of 10 less than the peak power in the argon range. XRD data presented below show a broader FWHM because they were were measured with a copper XRD filtered with 8.5-μm Kapton, whose response peaks at about 2 keV.

Table 3-1 summarizes the measured data for these experiments, grouped according to the diameter of the titanium wire. The x-ray yields in the argon and titanium spectral ranges are plotted as a function of implosion time in Figure 3-6. With no titanium wire, the argon K-shell yield peaks at about 24 kJ for an implosion time of 105 ns, in agreement with previous Double-EAGLE results (Reference 9). The addition of a titanium wire causes a decrease of about 20% in the argon yield, but the yield data show significant scattter. In the 4.5 to 5.0 keV spectral range measured by the Ross pair, the no-wire loads produce up to 0.25 kJ yield from argon K-shell recombination. Addition of a titanium wire increases the yield in the titanium range to about 1.0 kJ. These data have even more scatter (Figure 3-6b), and it is difficult to discern any consistent effects from the variation of wire diameter or argon pressure.

Two shots using a 5% krypton mixture in argon appear to produce much less titanium yield when compared to similar shots with 100% argon in the puff. Examination of the spectra shows that the ratios of H-like lines to He-like lines for both argon and titanium are smaller by a factor of 3 or more for the Kr/Ar mixtures. Thus, we conclude that the intense krypton L-shell radiation has lowered the plasma temperature, which in turn lowers the argon and titanium x-ray yields.
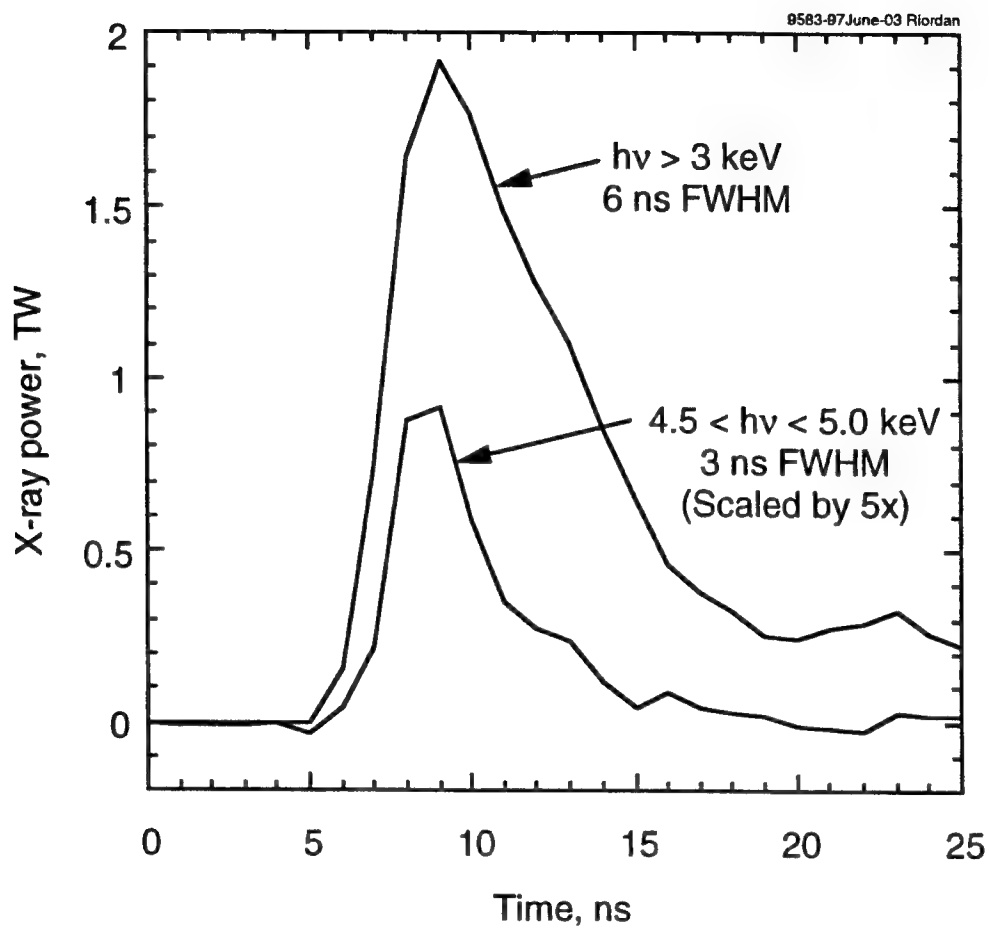
Figure 3-5. Comparison of radiated x-ray power in the argon (>3 keV) and titanium (4.5 to 5.0 keV) spectral ranges.
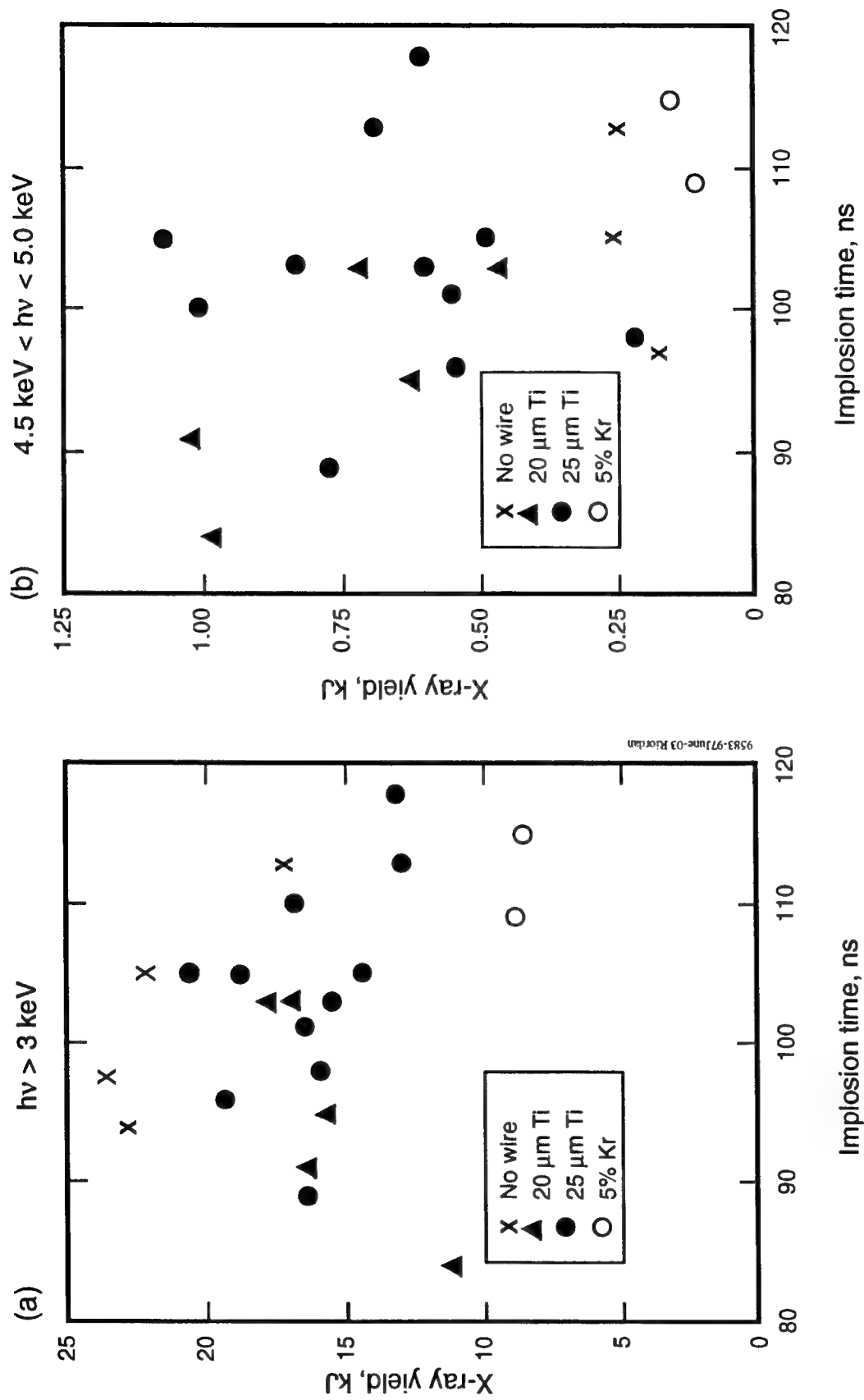
Figure 3-6. Measured K-shell x-ray yields versus implosion time; (a) argon and (b) titanium.

Table 3-1. Summary of experimental data for puff-on-wire loads.

Shot No.	Ti Wire Diam. (μm)	Ar Pressure (psia)	NS Timing (ns)	Peak Current (MA)	Implosion Time (ns)	XRD FWHM (ns)	X-ray Yield		
							> 3 keV (kJ)	4.5-5.0 keV (kJ)	> 5.0 keV (kJ)
3373	0	80	20	3.2	113	4	17.2	0.25	0.63
3374	0	80	-9	3.2	105	6	22.2	0.26	0.84
3404	0	50	8	3.0	94	8	23.0	-	-
3414	0	52	0	3.1	97	14	23.7	0.18	0.82
3375	20	55	10	3.0	95	10	15.6	0.62	0.35
3376	20	45	9	2.9	91	10	16.3	1.01	0.54
3378	20	35	-13	2.7	84	8	11.0	0.98	0.46
3379	20	80	-24	3.0	103	8	16.9	0.71	0.58
3420	20	65	-8	3.2	103	8	17.6	0.46	0.60
3363	25	80	-24	3.1	113	4	12.9	0.69	0.23
3364	25	80	-26	3.2	118	4	13.1	0.61	0.24
3367	25	80	-15	3.2	105	5	14.3	0.48	0.40
3369	25	65	-21	3.1	105	8	18.7	1.07	0.66
3370	25	60	25	3.0	110	8	16.8	1.00	0.42
3371	25	55	21	3.0	101	6	16.5	0.54	0.45
3372	25	55	25	3.0	103	10	15.4	0.59	0.32
3383	25	80	-8	3.3	103	4	20.9	0.83	0.36
3384	25	45	-4	2.9	89	16	16.3	0.77	0.27
3415	25	52	2	3.1	98	10	15.8	0.23	0.44
3416	25	48	-8	3.2	96	10	19.1	0.53	0.63
3417	25	75*	20	3.4	115	10	8.6	0.15	0.23
3419	25	75*	14	3.4	109	10	8.8	0.11	0.30

*5% Kr partial pressure

3.3 COMPARISON WITH THEORY.

Thornhill (Reference 10) has performed numerical simulations for the puff-on-wire load using a 1-dimensional MHD code coupled to the Double-EAGLE circuit model. This Lagrangian code allows no mixing of the elemental species across the boundary separating the titanium core from the argon shell, but it does use phenomenological transport coefficients for enhanced resistivity, thermal conductivity, and viscosity. A collisional-radiative equilibrium is used for ionization and a probability-of-escape approach is used for radiation transport.

Table 3-2 summarizes the model predictions for 3-cm long loads similar to those used in the Double-EAGLE experiments. The 20-μm wire produces the best titanium output, with a yield of 5 kJ above 4.5 keV. Figure 3-7 compares the predicted yields for the no-wire and 20-μm wire loads, plotted as a function of implosion time so that they can be compared to experiment. The
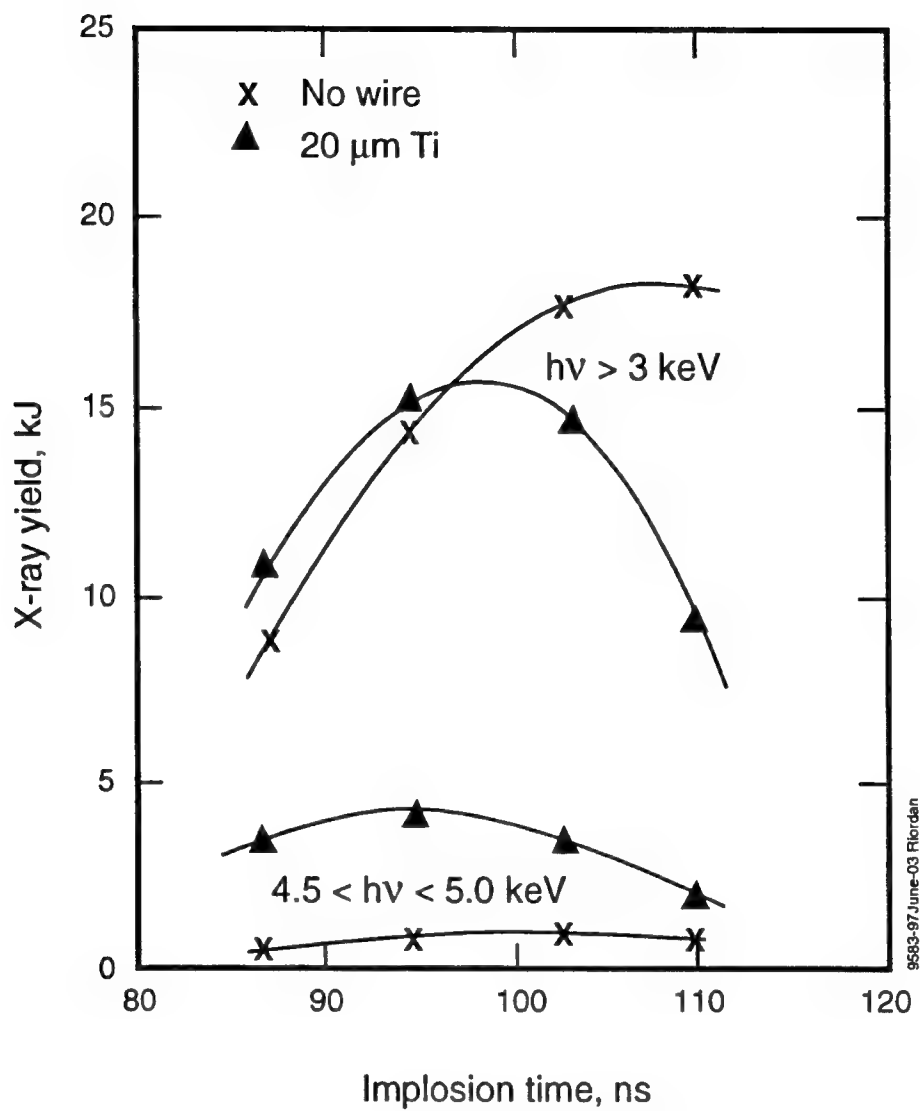
Figure 3-7. Theoretical x-ray yields versus implosion time, as predicted by 1D radiation hydrodynamic model (Reference 10).

theoretical model does an excellent job of predicting the optimum argon yield (>3 keV) and implosion time observed in the experiments with and without a wire (Figure 3-6).

Table 3-2. Summary of theoretical predictions for puff-on-wire loads (Reference 10).

Argon mass load (µg/cm)	100	150	200	250
Implosion time (ns)	87	95	103	110
Total coupled energy: η^*_{Ar}	2.5	2.0	1.9	1.6
Peak kinetic energy: η_{Ar}	0.9	0.7	0.6	0.5
Argon only				
Yield > 3 keV (kJ)	8.7	14.4	17.4	18.0
Yield > 4.5 keV (kJ)	0.9	1.5	1.8	1.8
Yield 4.5-5.0 keV (kJ)	0.3	0.5	0.6	0.6
Argon with 20 µm titanium wire				
Yield > 3 keV (kJ)	10.5	14.7	14.4	9.0
Yield > 4.5 keV (kJ)	4.2	5.1	4.8	2.7
Yield 4.5-5 keV (kJ)	3.0	3.6	3.0	1.5
Argon with 25-µm titanium wire				
Yield > 3 keV (kJ)	9.9	12.0	7.5	1.2
Yield > 4.5 keV (kJ)	4.1	3.0	2.0	< 0.1
Yield 4.5-5.0 keV (kJ)	3.0	1.4	1.1	< 0.1

The theory, however, is problematic for the titanium energy range (4.5 to 5.0 keV). Without a wire, the predicted yields are about a factor of two higher than observed, but the theoretical and observed optimum implosion times are in good agreement. With a titanium wire, the optimum theoretical yield of 3.6 kJ is a factor of three above the best measured yield, but the the experimental data have too much scatter to discern any trend with implosion time.

Measurements of the plasma conditions in the radiating core shed some light on the cause of the discrepancy between theory and experiment. Apruzese (Reference 11) has determined the electron temperature and ion densities in the core from the H-α/(IC+He-α) line ratio, x-ray power, and size of the radiating plasma. Table 3-3 compares the experimental plasma temperature and density to the predicted theoretical values. The measured temperatures of 1.8 keV for the argon and titanium components are only slightly higher than predicted. With 5% Kr in the gas mixture, the argon and titanium electron temperatures decrease to about 1.3 keV.

Table 3-3. Comparison of experimental measurements and theoretical predictions for electron temperature and ion density in the radiating plasma core.

	T_e, keV		N_i, ions/cm^3	
	Measured	Theory	Measured	Theory
Ar	1.8	1.5	3.3×10^{19}	3.3×10^{19}
Ti	1.8	1.7	$\leq 1 \times 10^{19}$	7.5×10^{19}

The experiment shows that the argon and titanium plasmas have the same temperature, unlike theory which predicts a 300-eV temperature difference. Thus, either the two plasmas are well-mixed or the thermal conductivity is much higher than expected. The ion density data suggest that mixing is the correct explanation. Table 3-3 shows excellent agreement between theory and experiment for the argon ion densities, but major discrepancies for the titanium densities. Theory predicts a titanium ion density of more than twice the argon ion density, while the experiment shows the titanium density is lower by a factor of >3. Since a low density core pinched inside a high-density shell is unphysical, we conclude that the argon and titanium plasmas are actually well-mixed.

The Lagrangian MHD model achieved high titanium density and yield because it does not allow diffusion or turbulent mixing of titanium ions into the lower density argon. In the experimental pinches, however, the core densities are too low to produce major yield improvements from marginal radiators like titanium. Furthermore, ACE-4 experiments using a neon puff on a copper wire also failed to demonstrate significant yield K-shell yields from copper (Reference 12). Thus, the puff-on-wire technique now appears less attractive as a means of generating the higher energy photons needed for a high-fidelity PRS.

SECTION 4

ALUMINUM/TITANIUM WIRE ARRAYS

By placing the titanium in wires at a finite initial diameter rather than on axis, we expected to improve the coupled kinetic energy compared to that achieved in the puff-on-wire configuration. Furthermore, by applying the titanium as a coating on aluminum wires we hoped to create a hotter core plasma, as demonstrated with the magnesium-coated aluminum wire arrays. The experiments described below systematically investigated a variety of wire array loads designed to optimize the titanium x-ray output.

The aluminum/titanium wire arrays did increase the titanium K-shell yield slightly compared to the puff-on-wire loads, but the optimum titanium yield obtained with 100% Ti wires was only 1.2 kJ. As the titanium fraction was decreased, the titanium-yield decreased linearly and the aluminum yield increased sharply. Arrays containing a mixture of pure titanium and pure aluminum wires appeared to perform slightly better than coated wires, but the dynamics of these mixed element loads is not understood.

4.1 WIRE ARRAY LOADS.

We designed the wire array loads to independently vary a number of key load parameters believed to be important for optimizing the titanium x-ray yield and spectral mix. In particular, we varied the following parameters: titanium mass fraction, wire array mass, number of wires, and wire array diameter. Furthermore, we also tested several arrays consisting of a mixture of pure titanium and aluminum wires to distinguish coating effects from elemental composition effects.

The wire arrays consisted of 20-mm-long wires mounted in hardware similar to that described in Section 1.1. An array diameter of 25.5 mm was selected for most of the shots because it produced optimum aluminum x-ray yields of 40 to 50 kJ in previous experiments. The baseline load contained 12 wires with a total mass of nearly 200 μg/cm. We also tried several shots with a larger, 35.5-mm-diameter array to provide a higher implosion velocity. In theory these loads should couple more kinetic energy per ion and improve the titanium heating.

The titanium coating was applied to the aluminum wire core using an evaporative deposition process. By controlling the thickness of the coating we varied the titanium mass fraction from 18% to 48%. Wire array loads with 0% and 100% titanium were also fabricated using pure, uncoated wires. Table 4-1 summarizes the individual wires used in these experiments. The first

41

five wires were used to vary the titanium fraction while maintaining an array mass near 200 μg/cm. The last three wires maintained a constant 33% titanium fraction and were used in scans of the array diameter, mass and wire number.

Table 4-1. Wires for titanium/aluminum loads.

Titanium Fraction (%)	Aluminum Diameter (mils)	Titanium Coating (μm)	Wire Mass (μg/cm)
0	1.1	-	16.6
18	1.0	0.80	16.7
33	0.9	1.60	16.7
48	0.8	2.50	16.9
100	-	20.3 dia	14.7
33	0.7	1.25	10.1
33	0.8	1.40	13.1
33	1.0	1.80	20.7

The Double-EAGLE generator was operated with the Marx bank charged to 60 or 61 kV for all of these experiments. The peak load current was 4 to 5 MA, depending upon the mass and diameter of the load. The current waveforms are similar to those of Figure 1-2.

4.2   X-RAY MEASUREMENTS.

The x-ray yield above 1.5 keV (predominately aluminum K-shell)) was measured using calorimeters and PCDs filtered with 8.5-μm Kapton plus 4.2-μm Kimfol. As discussed in Section 1.2, we corrected the yields using a constant filter transmission of 37%, which was evaluated at a photon energy of 1.70 keV between the He-α and H-α resonance lines. This filter correction does not properly treat the titanium K-shell x-rays, whose filter transmission is 95%. Nevertheless, this approach overestimates the >1.5-keV yield by only 1 to 2 kJ because the titanium yield is so small.

The titanium K-shell x-ray yield in the 4.5-to-5.0-keV band was measured differentially using a pair of PCDs with Ross filters, as described in Section 3-2. The Ross pair filters were 15-μm scandium and 25-μm titanium, but each was combined with an additional layer of 8.5-μm Kapton for these experiments. To calculate the x-ray yield in the pass-band we used a differential filter transmission of 50% evaluated at the 4.75-keV photon energy of the dominant He-α line. On shots with no titanium, the Ross pair diagnostic gave negligible yield in the 4.5-5.0 keV band.

Table 4-2 summarizes the key data for the titanium/aluminum wire array experiments. In general, the x-ray yield with 100% Al was 40 to 50 kJ, consistent with the yields reported in Section 1.3. The optimum titanium yield of 1.2 kJ was obtained with 100% Ti and was slightly higher than the 1.0 kJ achieved using the puff-on-wire configuration. For consistency, we have used only the calorimeter data for the aluminum yields in the discussion below, because uncalibrated PCDs were used on the early shots.

Table 4-2. Summary of experimental data for aluminum/titanium wire arrays.

Shot No.	Ti Frac. (%)	Array Dia. (mm)	Wire No.	Mass (µg/cm)	Peak Current (MA)	N-S Timing (ns)	Implosion Time (ns)	PCD FWHM (ns)	Aℓ X-ray Yields Cal (kJ)	Aℓ X-ray Yields PCD (kJ)	Ti Yield Ross Pr. (kJ)
3519	0	25.5	12	199	4.5	-10	100	46	53.7	-	-0.15
3562	0	25.5	12	199	-	-21	96	47	39.9	33.0	-0.04
3572	18	25.5	12	200	4.5	2	91; 100	29	37.3	-	0.65
3573	18	25.5	12	200	4.4	22	92; 109	24	32.5	-	0.42
3568	18	25.5	12	200	-	29	90; 100	37	24.5	22.2	0.45
3524	33	25.5	12	200	4.4	11	87; 109	34	22.8	-	0.83
3525	33	25.5	12	200	4.4	10	86; 93	26	26.1	-	0.79
3567	33	25.5	12	200	-	16	90	33	18.4	18.0	0.57
3526	48	25.5	12	203	4.5	-8	95; 112	28	16.8	-	0.56
3541	48	25.5	12	203	4.5	4	100; 115	17	10.7	9.0	0.44
3565	48	25.5	12	203	-	-1	93	31	12.4	13.5	0.65
3520	100	25.5	12	176	4.3	5	95; 110	15	-	-	1.26
3521	100	25.5	12	176	4.4	6	95; 105	28	-	-	1.20
3563	100	25.5	12	176	-	-1	90; 103	41	-	-	1.13
3542	33	25.5	12	121	4.4	11	98	26	14.2	11.7	0.80
3543	33	25.5	12	121	4.2	-15	100	30	13.3	10.9	0.60
3545	33	25.5	12	157	4.4	17	91; 106	30	12.0	12.7	0.45
3552	33	25.5	12	157	-	-6	92	34	17.2	15.6	0.74
3550	33	25.5	12	248	-	21	89; 112	19	15.9	14.5	0.35
3553	33	25.5	12	248	-	-10	88; 105	29	18.0	15.1	0.43
3544	33	25.5	15	197	4.7	10	97; 110	20	8.6	8.5	0.16
3549	33	25.5	15	197	-	-12	96; 110	26	18.0	18.3	0.67
3551	33	25.5	20	202	-	9	108	17	14.6	14.2	0.43
3554	33	25.5	20	202	-	-3	101	17	11.6	11.1	0.33
3559	47	25.5	6 Aℓ; 6 Ti	188	-	8	91	37	14.2	13.5	0.92
3564	47	25.5	6 Aℓ; 6 Ti	188	-	-20	92; 100	38	15.9	14.1	0.91
3561	23	25.5	9 Aℓ; 3 Ti	191	-	-5	91	36	20.6	16.5	0.45
3555	33	35.5	12	121	-	-13	99	51	6.9	6.8	0.46
3556	33	35.5	12	157	-	-19	112	55	10.6	8.3	0.34
3557	33	35.5	12	200	-	19	96; 102	49	10.6	7.5	0.31
3558	100	35.5	12	176	-	25	105	25	-	-	1.18

Figure 4-1 shows the titanium K-shell spectra for 100% and 18% Ti loads; the spectrum varies only slightly for other loads. The dominant ionization states are He-like and Li-like, with a negligible fraction of H-like. The absence of significant H-like lines indicates that the wire array plasmas are cooler than the puff-on-wire plasmas discussed in the previous section (Figure 3-3); quantitative measurement of the titanium plasma temperature is difficult.

Figure 4-2 shows typical pulse shapes for the aluminum and titanium x-ray powers measured with Kapton-filtered PCDs and Ross-pair PCDs, respectively. The x-ray pulse shapes for titanium/aluminum and pure titanium wires usually show a pronounced precursor that has not been observed in previous mixed-element PRS. The magnitude of the precursor is typically 20 to 30% of the peak, but occasionally as high as 50%. The multiple implosion times in Table 4-2 refer to the extrapolation of the leading edges of the precursor and main pulse to the baseline.

For arrays containing nearly 50% Ti, the precursor appears to be higher for mixed wires than for coated wires (Figure 4-2), leading to a broader FWHM for the aluminum x-ray power. The titanium x-ray power pulse width is 26 to 28 ns FWHM, much longer than that of the puff-on-wire loads. The longer x-ray pulse widths of the wire arrays probably results from the inferior cylindrical symmetry inherent in the wire arrays. The prolonged titanium pulse also suggests that the plasma temperature has a broad temporal peak consistent with the stagnation of a thick, poorly-defined shell.

4.3   LOAD PARAMETER STUDIES.

Elemental composition is the most important factor in determining the x-ray output in both the aluminum and titanium K-shell ranges. Figure 4-3 shows the dependence of the x-ray yields and pulse width upon the titanium mass fraction; array diameter, mass, and wire number have been held constant. The titanium yield increases roughly linearly with increasing titanium fraction, as expected. The aluminum yield and pulse width, however, decrease sharply with increasing titanium fraction. With 48% Ti, the aluminum yield has decreased by a factor of three and the pulse width by a factor of two. We suspect that the much of the plasma energy is being radiated in the titanium L-shell lines below 1 keV, but we did not field diagnostics for this spectral range.

Inserting the titanium as a mixture of alternating pure wires rather than as a coating appears to be beneficial. Figure 4-3 also shows that a wire mixture with 47% Ti (6 Al and 6 Ti wires) gave a longer pulse and a higher titanium yield than a comparable 48% Ti coated-wire array. A single 23% Ti shot with 9 aluminum and 3 titanium wires failed to confirm this result, however.
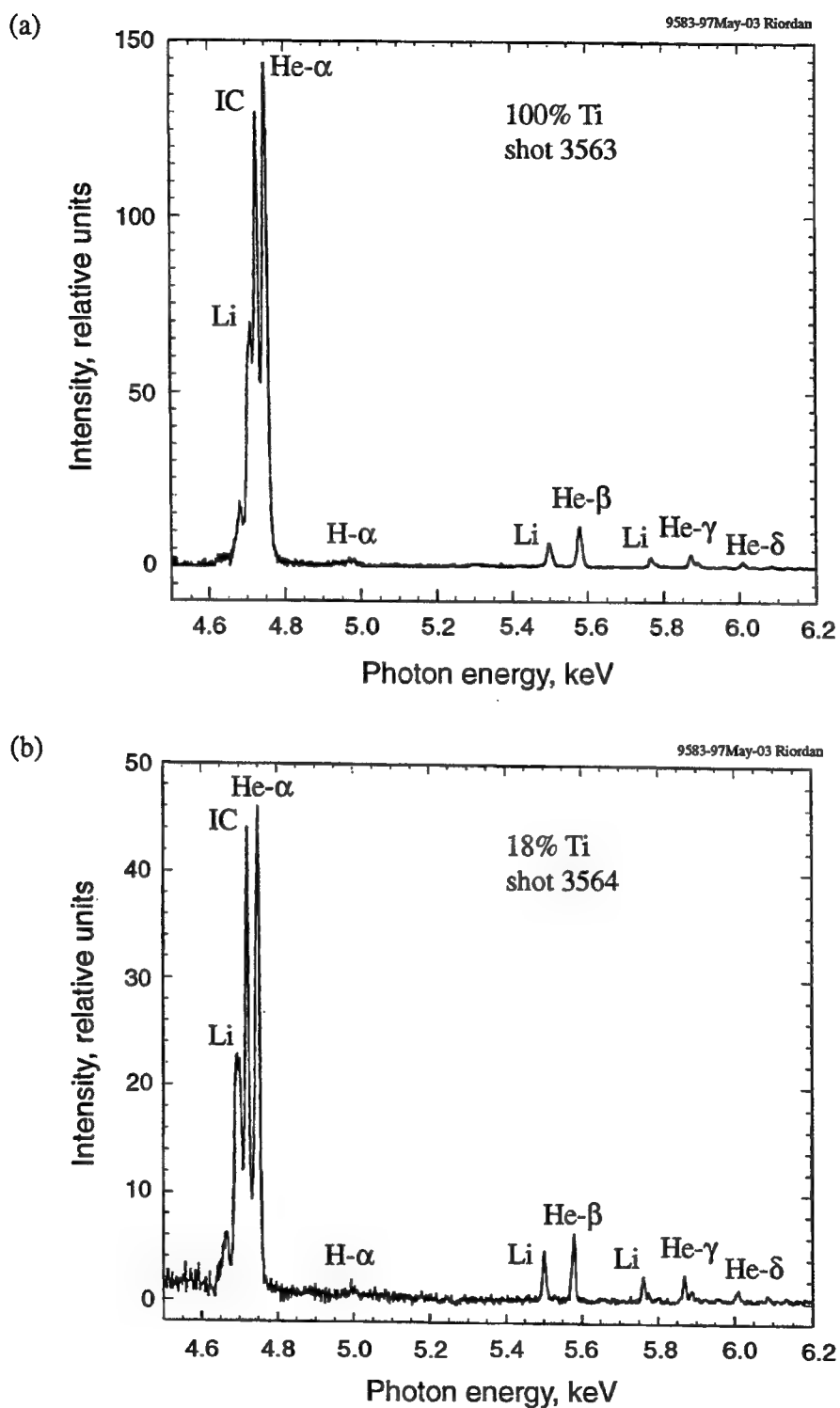
44

Figure 4-1. Measured K-shell x-ray spectra for wire arrays with (a) 100%
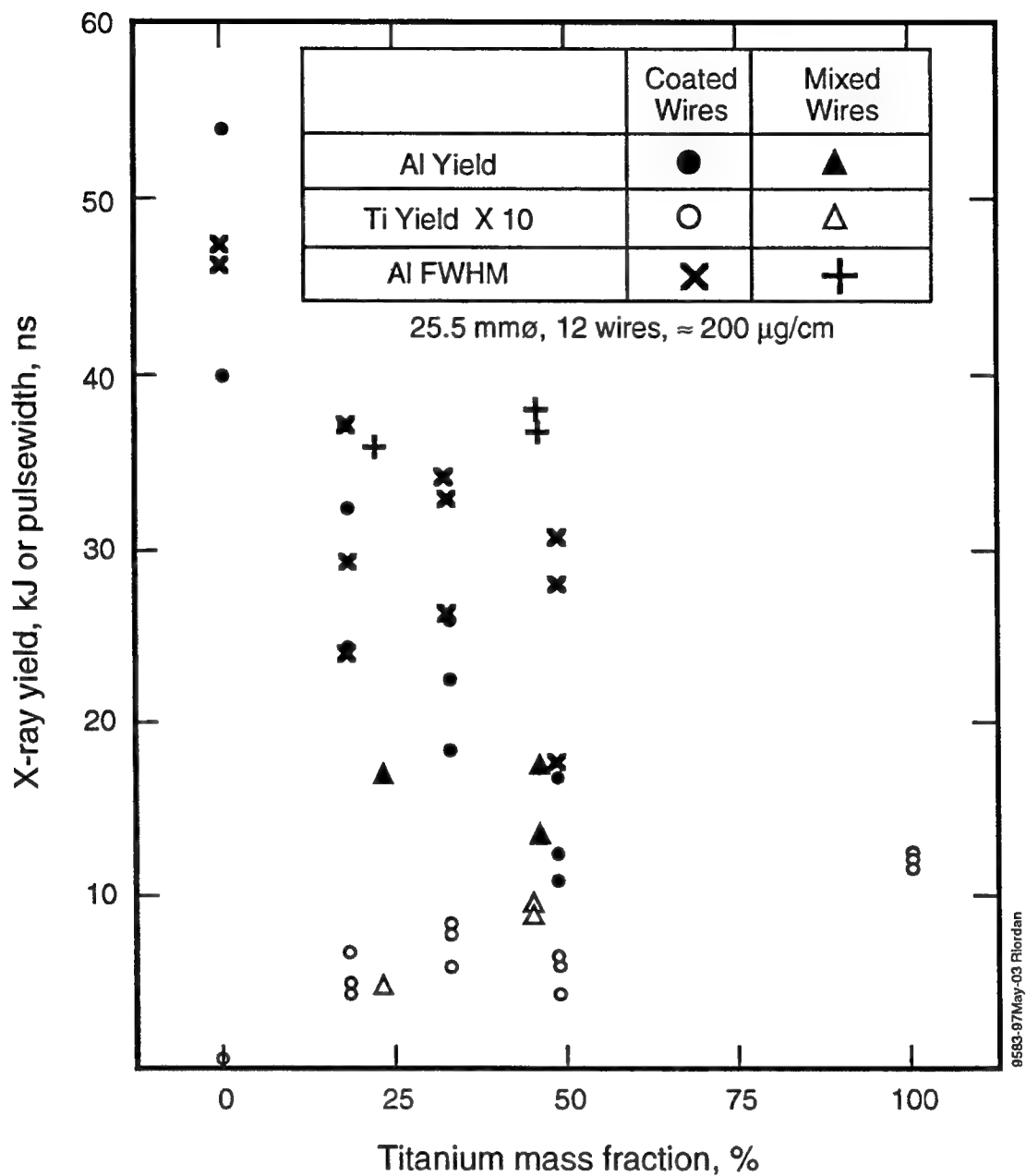Ti and (b) 18% Ti.

Figure 4-2. X-ray yields and pulse width versus titanium mass fraction for 12-wire arrays with 25.5-mm diameter and a mass of nearly 200 µg/cm.
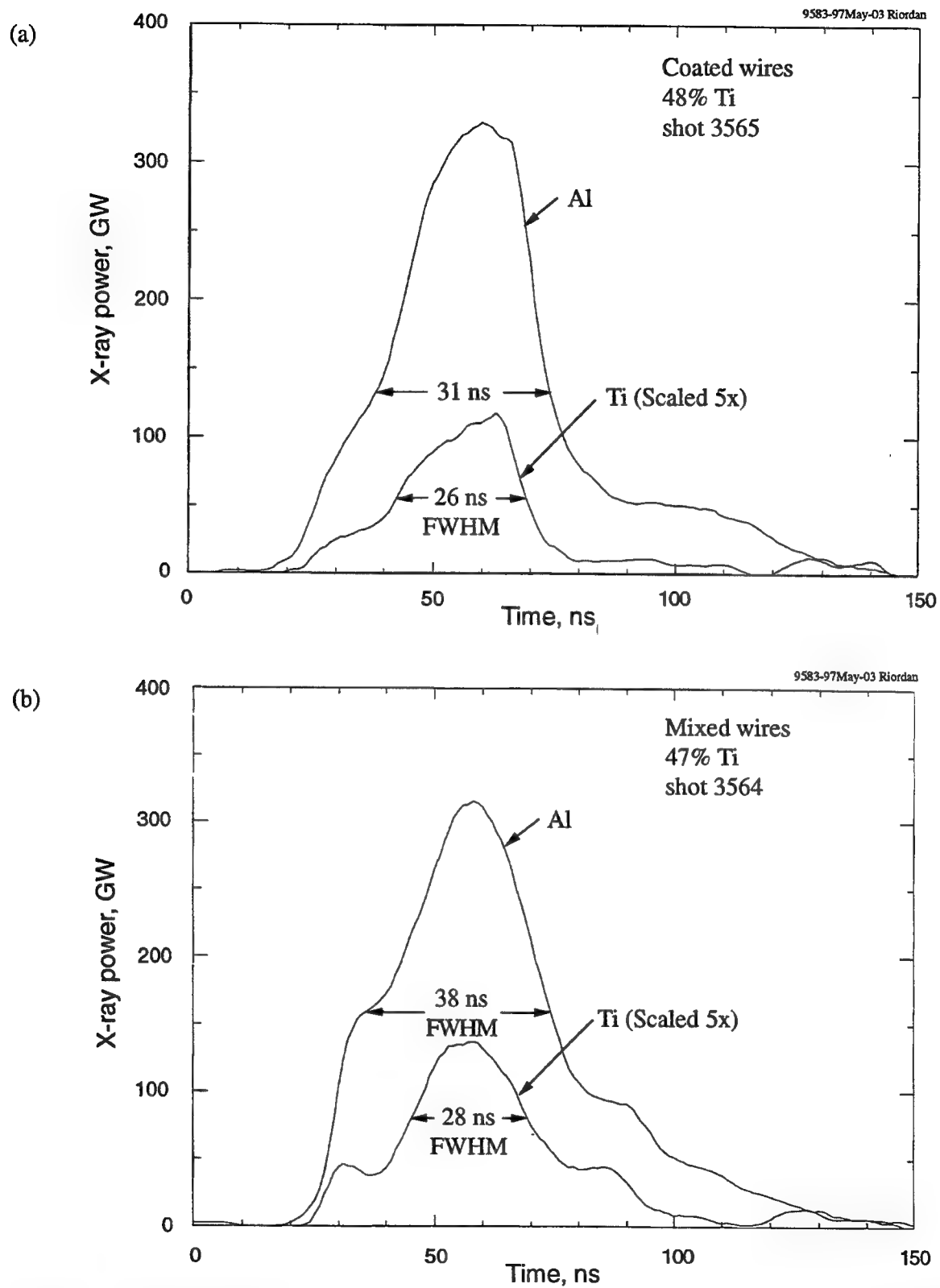
Figure 4-3. X-ray power in the aluminum and titanium spectral ranges for (a) coated wires with 48% Ti and (b) mixed wires with 47% Ti.

47

The mass and diameter of the wire array also affect the x-ray output. Figure 4-4 shows that the baseline mass of 200 µg/cm produced the maximum aluminum yield and pulse width. The titanium yield appears less dependent upon the mass, but does fall off for large masses where the kinetic energy per ion is too low. Contrary to expectations, the 35.5-mm arrays did not perform as well as the 25.5-mm arrays. Both the aluminum and titanium yields are below the comparable values obtained with the same 33% Ti fraction in 25.5-mm arrays (Figure 4-4). The aluminum x-ray pulse width is about 50 ns for the larger arrays and <35 ns for the smaller arrays. Nevertheless, with 100% titanium wires, the 25.5-mm and 35.5-mm array appear to produce comparable x-ray yields of about 1.2 kJ (Table 4-1).

We also observed output variations with wire number, confirming the previous observation that start-up effects play a significant effect upon the x-ray output (Section 2.3). Optimum yields for both aluminum and titanium x-rays are obtained with 12-wire arrays, even though their symmetry is clearly inferior to that of 15- and 20-wire arrays (Figure 4-5). The x-ray pulse width, however, decreases by nearly a factor of two as the number of wires is increased from 12 to 20.

Time-gated x-ray images can help in understanding the dependence of the x-ray output upon array diameter and wire number. The images shown in Figure 4-6 are filtered by 8.5-µm Kapton plus 10-µm titanium. These filters have a combined transmission of only 0.03% at 1.7 keV, so the images are indicative of the higher spectral components; the characteristic 37% transmission occurs at 3.6 keV. Figures 4-6a and 4-6b show the effects of increasing wire array diameter. The final compressed diameter for the 35.5-mm array is about twice as large as the final diameter for the 25.5-mm array. Thus, the reduced density in the radiating pinch explains the lower x-ray power and yield observed with the larger diameter array. Figures 4-6a and 4-6c show the effect of increasing wire number. The 20-wire load is clearly more stable, probably because of the improved symmetry. The stable plasma radiates its stagnation energy at higher power, producing a shorter x-ray pulse.

The low x-ray yields achieved with the larger-diameter array confirm the theoretical prediction (Reference 8) that density is more critical than temperature for titanium x-ray production. Nevertheless, much remains to be learned about the physics of wire array PRS created from mixed elements with widely separated atomic numbers. The titanium coating failed to achieve higher core temperatures than the puff-on-wire loads, indicating that the coating/core dynamics is different from that observed with the magnesium coating. The fact that wire mixtures performed slightly better than coated wires suggests that alloy wires may actually be preferable; alloys are certainly easier to fabricate than coatings.

X-ray yield, kJ or pulsewidth, ns vs **Wire array mass, µg/cm**

33% Ti
12 wires

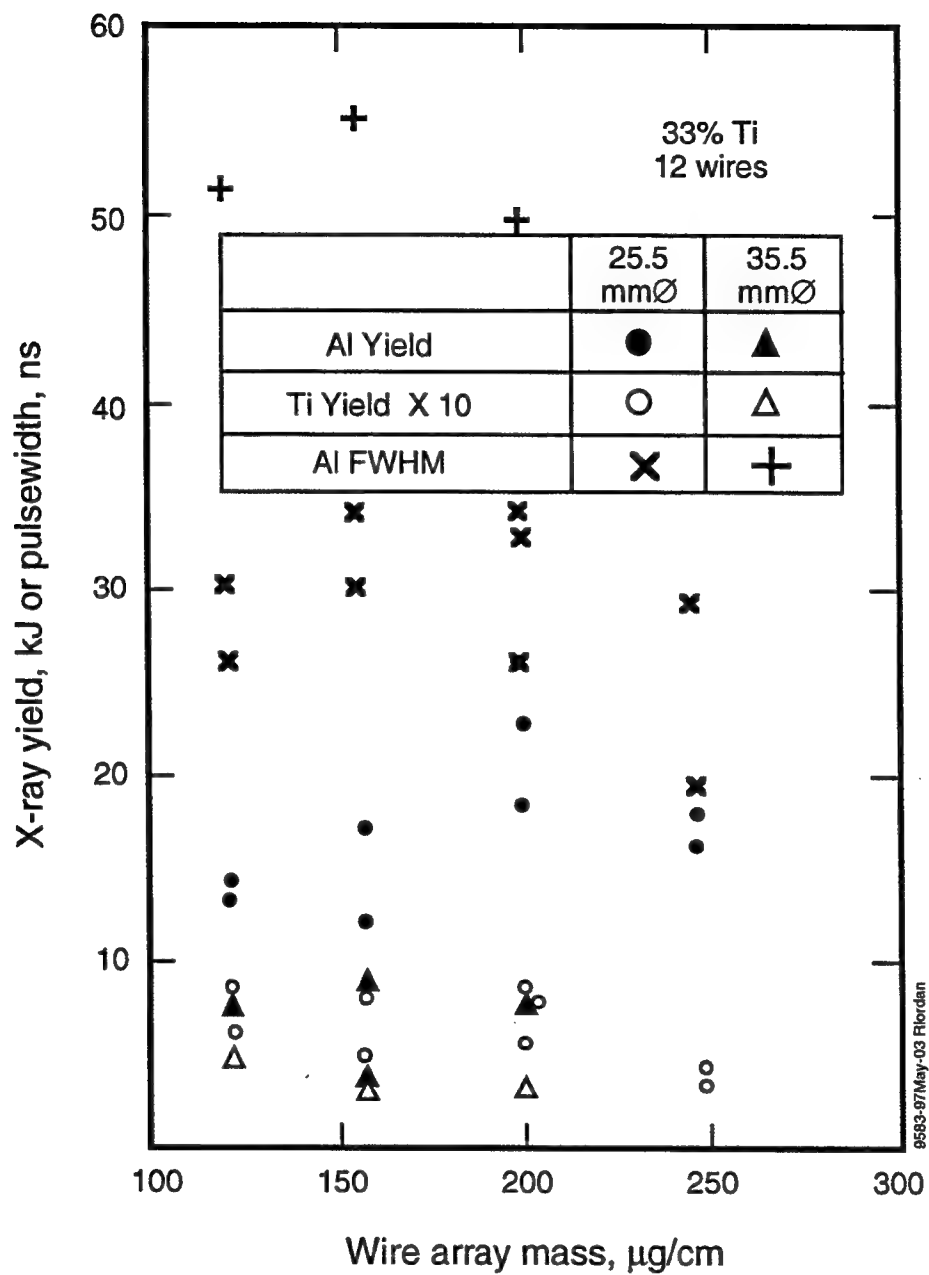|	25.5 mmØ	35.5 mmØ
Al Yield	●	▲
Ti Yield X 10	○	△
Al FWHM	✕	+

Figure 4-4. X-ray yields and pulse width versus wire array mass for 12-wire arrays with 33% Ti.

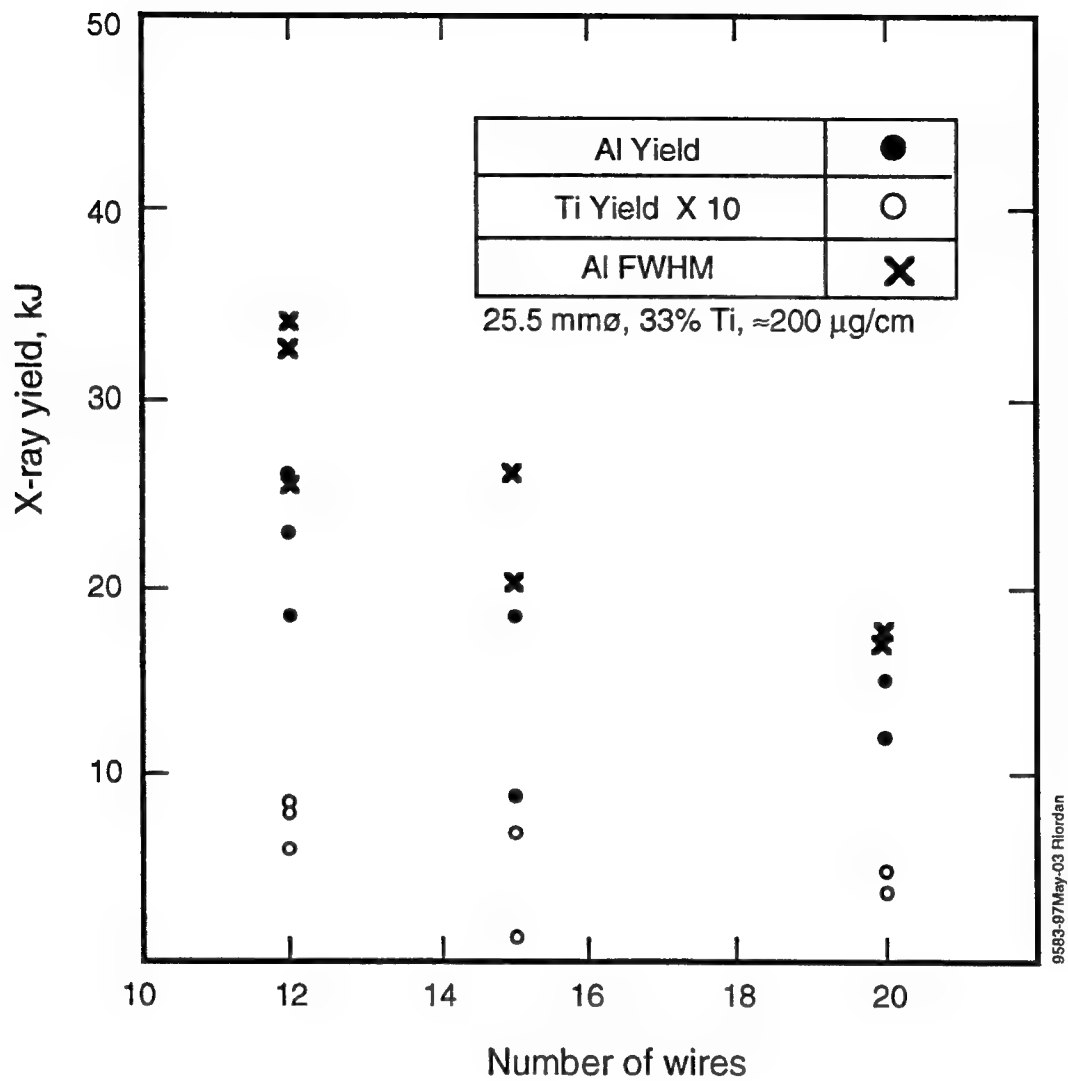**Figure 4-5.** X-ray yields and pulse width versus wire number for 25.5-mm-diameter arrays with 33% Ti and a mass of nearly 200 μg/cm.

(a) Shot 3567, 25.5 mm ø, 12 wires

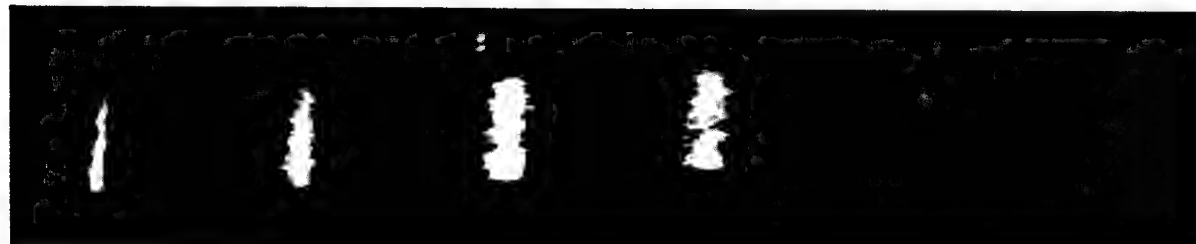
9583-97May-03 Riordan

(b) Shot 3557, 35.5 mm ø, 12 wires

9583-97May-03 Riordan

(c) Shot 3551, 25.5 mm ø, 20 wires

9583-97May-03 Riordan

Time ⟶

5 ns frames, 10 ns apart

Figure 4-6. Gated x-ray images for 33% Ti arrays with (a) 25.5-mm diameter, 12 wires; (b) 35.5-mm diameter, 12 wires; and (c) 25.5-mm diameter, 20 wires.

SECTION 5

MIXED-ELEMENT WIRE ARRAYS ON SATURN

We have already described experiments using mixed-element wire arrays on Double-EAGLE to overcome opacity limits (Section 2) and improve spectral fidelity (Section 4). In this section, we describe similar experiments to determine how mixed-element loads scale to the higher mass and current available on the Saturn generator at the Sandia National Laboratories. Magnesium-coated aluminum wires were used to investigate the reduction of opacity for elements of similar atomic number, while a potassium chloride coating on aluminum wires was used to enhance the spectral intensity at higher photon energy.

The Saturn aluminum K-shell x-ray yields were comparable to those produced on Double-EAGLE, despite the higher current and load mass. Adding a small fraction of magnesium increased the total K-shell yield by 16% (magnesium alloy) to 24% (magnesium coating). Adding potassium chloride increased the yield above 2.7 keV only slightly, but did cause a significant reduction in the combined K-shell yield. Spectral measurements show an intense aluminum free-bound continuum with >1 keV temperature that radiates strongly at the higher energy range. There is also evidence of a steep radial temperature gradient in the K-shell radiating core.

5.1 WIRE ARRAY LOADS.

The wire array loads used in these experiments were variations of a baseline aluminum array already developed for Saturn. All loads consisted of 30 wires arranged in a circular array with a 24-mm diameter and a 20-mm length. The nominal 410-μg/cm array mass was about 40% higher than the primary mass used for the aluminum/magnesium experiments on Double-EAGLE. The current return cage consisted of 8 posts in a 54-mm diameter array, which provided better magnetic field symmetry (1% asymmetry ratio) than Double-EAGLE. Figure 5-1 illustrates the Saturn wire load configuration.

Because of the limited number of shots available for these experiments, the loads were designed primarily to vary a single parameter: elemental composition. As shown in Table 5-1, we used aluminum alloys containing 1% and 6% Mg; higher magnesium fractions of 19% and 36% were obtained by using magnesium coatings on aluminum core wires. Potassium chloride coatings were also applied to the core aluminum wire to produce mass fractions of 19% and 36% KCl. To minimize oxidation of the coating, the wires were stored in dry air. To further protect the
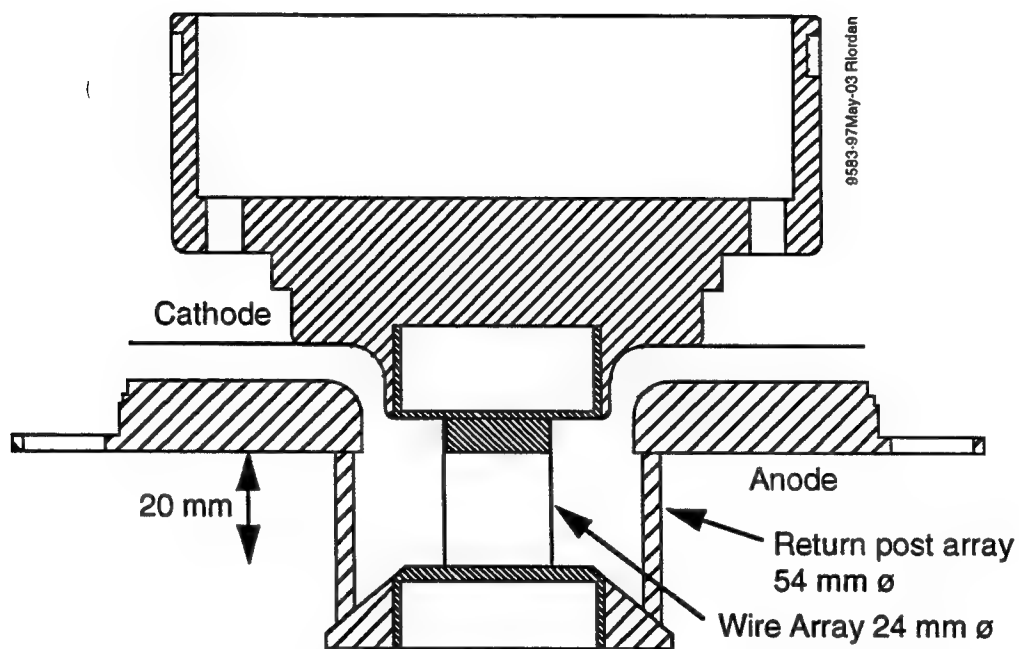
52

Figure 5-1. Wire array configuration on Saturn.

hydrophilic salt, the KCl-coated wires had an additional outer coating of 0.1-μm titanium, which increased the total mass by <3%.

Table 5-1. Mixed-element wires for Saturn experiments.

Nominal Wire Load	Core Wire Diameter (in.)	Core Wire Composition	Coating	Array Mass (μg/cm)
1% Mg	0.0010	99% Al, 1% Mg	–	410
6% Mg	0.0010	94% Al, 6% Mg	–	410
19% Mg	0.0009	100% Al	1.9 μm Mg	410
36% Mg	0.0008	100% Al	3.3 μm Mg	410
19% KCl	0.0009	99% Al, 1% Mg	1.7 μm KCl + 0.1 μm Ti	420
36% KCl	0.0008	99% Al, 1% Mg	3.3 μm KCl + 0.1 μm Ti	420

5.2 X-RAY MEASUREMENTS.

The K-shell x-ray yield and power were measured using PCDs filtered to reject the sub-keV radiation; filter transmission curves are shown in Figure 5-2. For aluminum/magnesium x-rays, the filters consisted of 8-μm beryllium plus 1-μm Parylene-N; for potassium and chlorine x-ray measurements a 7-mm titanium filter was used to reject the aluminum and magnesium lines. In all cases the yields were corrected using a spectrally-weighted transmission calculated from the measured spectra. Total radiated yields were measured with an unfiltered bolometer, and the total power pulse shape was determined using a vitreous carbon XRD filtered with 5-μm Kimfol. All yields were multiplied by a factor of 2.08 to correct for occlusion along the diagnostic line of sight, which is tilted at an angle of 55 degrees to the array axis.

Figure 5-3 shows load current and x-ray power waveforms for a typical shot with 19% Mg wires. The Saturn current peaked at 7 MA, compared to 4 MA on Double-EAGLE. The implosion time was 55 ns, compared to 80-90 ns on Double-EAGLE. The K-shell x-ray power and total radiated power peaked at 2 TW and 8 TW, respectively. Table 5-2 summarizes the key x-ray data for all good shots in the Saturn test series.

The baseline array of aluminum (actually 1% Mg) wires provides a useful point of comparison between Saturn and Double-EAGLE. The wire diameters were identical (0.001 inch) and the array diameters were nearly identical (24 and 25 mm respectively). The Saturn array, however, had more wires (30 versus 18) and 67% higher mass. Nevertheless, both loads produced an average K-shell x-ray yield of 50 kJ, despite the higher current and mass on Saturn. As discussed in the
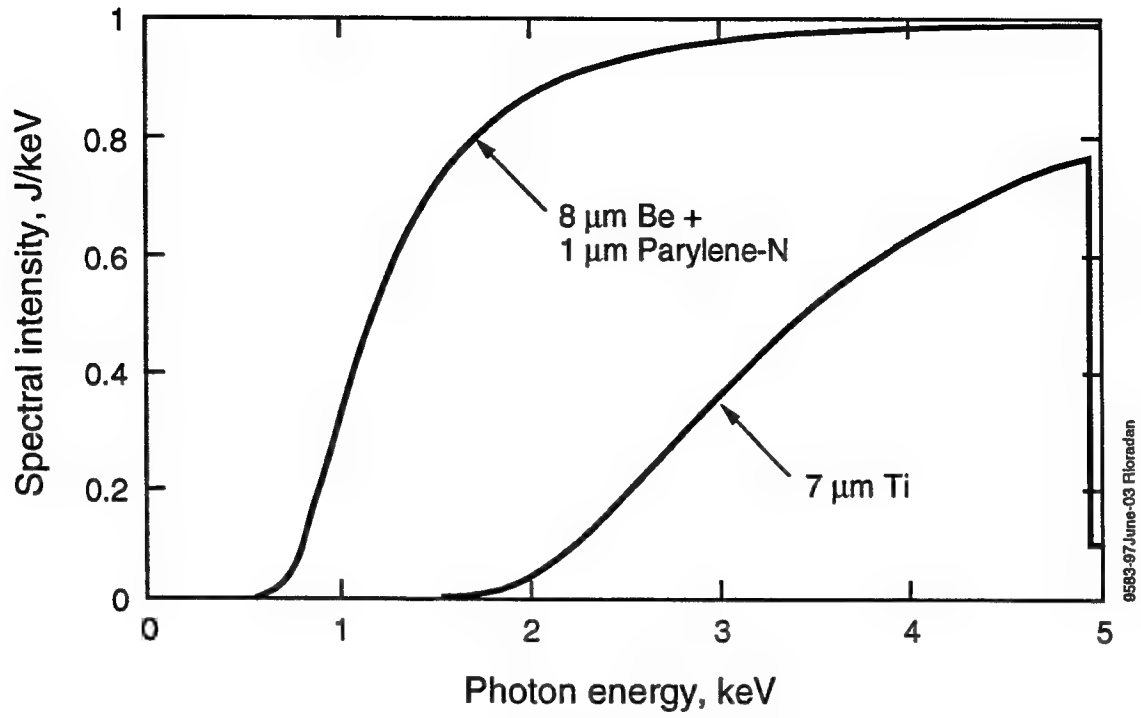
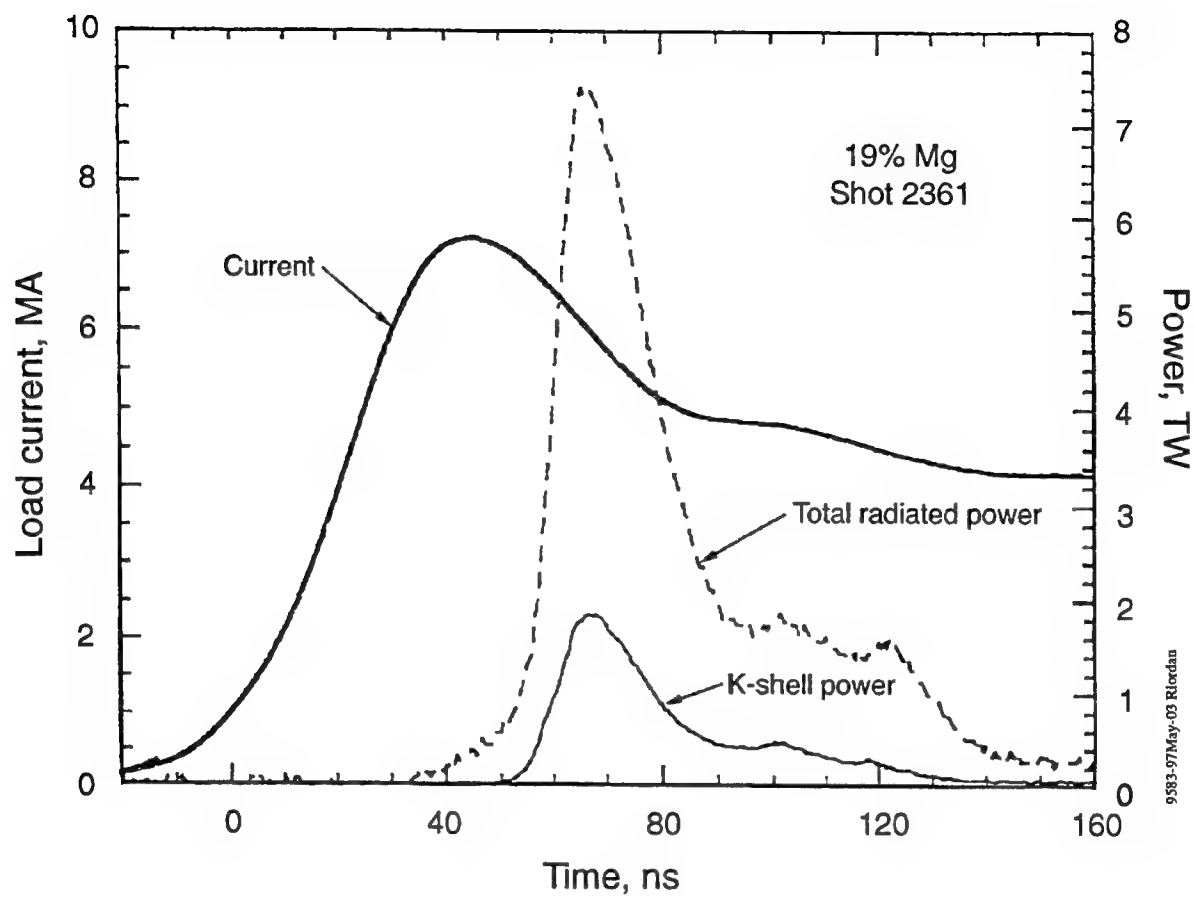**Figure 5-2. Calculated transmission curves for Saturn PCD filters.**

Figure 5-3. Current and x-ray waveforms for 19% Mg wire array on Saturn.

following section, we believe that the plasma temperature on Saturn was too high and that the ions were too highly ionized for optimum emission of aluminum K-shell x-rays.

Table 5-2. Summary of x-ray data for mixed-element wire arrays on Saturn.

Shot No.	Wire Load	Peak Current (MA)	Implosion Time (ns)	X-ray FWHM (ns)	K-shell Yield (kJ)	> 2.7 keV Yield (kJ)	Total Rad. Yield (kJ)
2369	1% Mg	6.5	46	25	54	12	233
2370	1% Mg	6.7	49	30	46	9	209
2360	6% Mg	6.9	54	25	62	13	253
2361	19% Mg	7.2	54	20	58	13	249
2364	37% Mg	6.9	52	23	48	–	203
2365	19% KCl	7.1	54	15	40	12	254
2366	19% KCl	7.1	50	18	46	13	252
2367	36% KCl	7.0	51	25	30	13	305
2368	36% KCl	7.0	50	22	34	13	284

5.3   ALUMINUM/MAGNESIUM RESULTS.

The Saturn experiments appear to confirm previous experiments showing that the addition of a small magnesium fraction can increase the total K-shell x-ray yield. As shown in Figure 5-4, the 6% Mg wires gave a K-shell yield of 62 kJ, compared to an average of only 50 kJ for the baseline load with 1% Mg wires. Using coated wires for higher magnesium content, the total K-shell yields were 58 kJ and 48 kJ, respectively, for 19% and 36% Mg wires. Thus, the magnesium/ aluminum wires have increased the K-shell yield by 16% to 24% on Saturn, compared to a 19% increase in mean yield observed with 20% Mg wires on Double-EAGLE. At still higher magnesium fractions there was no significant enhancement of the K-shell yield on either Saturn or Double-EAGLE. Because of the limited number of Saturn shots, it is impossible to determine whether there are any significant differences between Saturn and Double-EAGLE in the yield increase or the optimum magnesium fraction.

K-shell x-ray spectra for magnesium-coated aluminum wire arrays show that the relative strength of the magnesium lines increased with magnesium mass fraction as expected (Figure 5-5). These spectra also show that the magnesium and aluminum are both predominantly H-like on Saturn. On Double-EAGLE, however, the aluminum/magnesium spectra showed the aluminum plasma to be predominantly He-like (i.e., cooler) unless the aluminum was present at the wire surface.
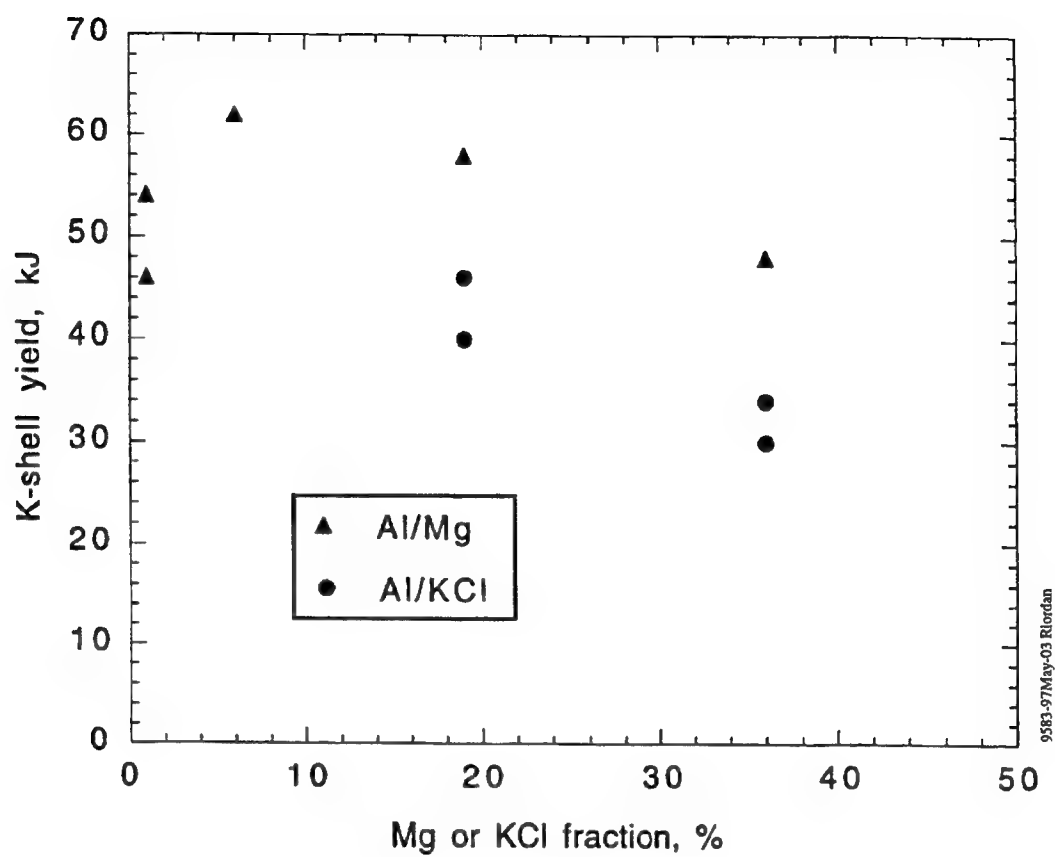
Figure 5-4. Measured K-shell x-ray yields versus Mg or KCl mass fraction.
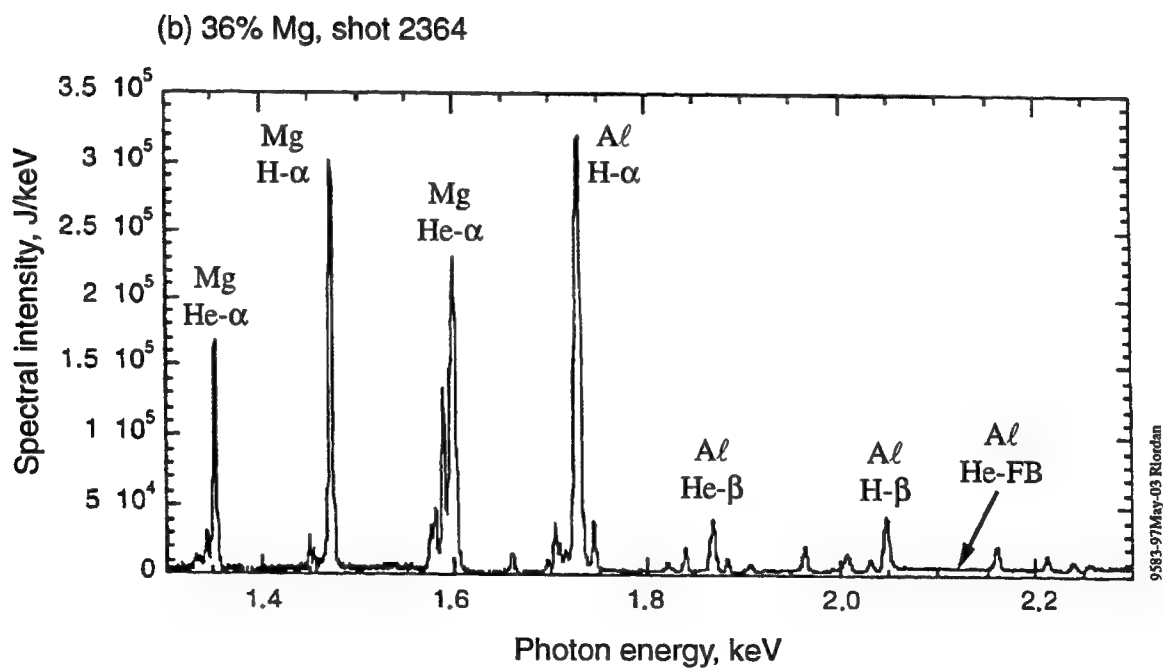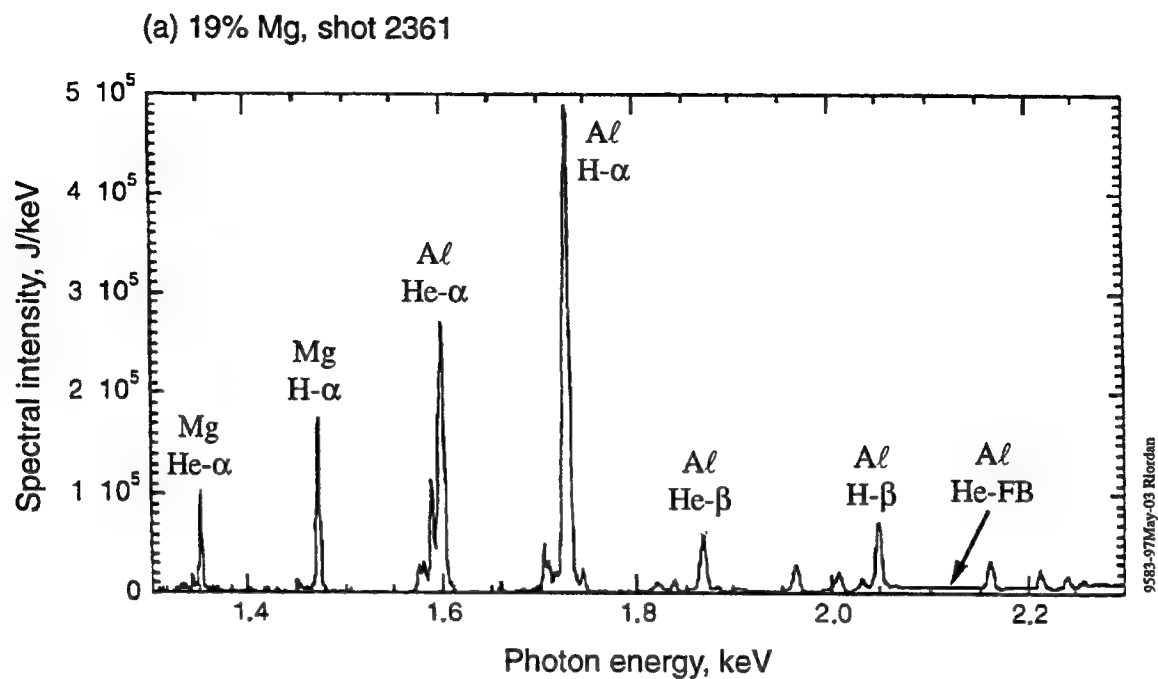
Figure 5-5. Measured spectra for aluminum wires with magnesium coating; (a) 19% Mg and (b) 36% Mg.

The Saturn spectra show a significant free-bound continuum, which contains >35% of the x-ray energy. The x-ray energy in the free-bound continuum measured on Double-EAGLE was typically much lower (about 5%), presumably because of the lower plasma density. Because the continuum has lower opacity than the lines, we expected that the magnesium/aluminum mixture would have been less effective in increasing the K-shell yield on Saturn than on Double-EAGLE. Nevertheless, a yield increase of about 20% was observed on both generators.

Electron temperature in the K-shell-radiating core can be estimated from the time-integrated spectra of Figure 5-5 using several methods. Apruzese measured a temperature from the ratio H-α to He-α plus intercombination lines for both magnesium and aluminum, using the method of Coulter et al (Reference 13). L'Eplattenier (Reference 14) inferred the temperature from the slope of the He-like and H-like free-bound continua, whose opacity is much lower than that of the lines. Table 5-3 summarizes the temperature estimates, which show that the temperature appears to vary inversely with the opacity of the spectral feature used in its estimate. Thus, the continuum temperatures of approximately 1 keV represent regions closer to the center of the plasma, and are a lower bound to the maximum temperature at the center of the pinch.

Table 5-3. Electron temperature for Saturn aluminum/magnesium
wire arrays (References 11 and 14).

Shot No.	Mg Fraction (%)	Electron Temperature (eV)			
		Mg Lines	Al Lines	He-like Al Continuum	H-like Al Continuum
2369	1	–	770	650	1150
2370	1	–	680	550	1100
2360	6	–	500	700	1000
2361	19	630	720	600	1150
2364	36	580	480	800	1100

Even the higher order H-like aluminum lines are optically thick in the Saturn plasmas. Figure 5-6 shows a comparison of two measured spectra and RATION calculations for an optically thin spectrum. Because the lines are close in energy, the theoretical line ratios are insensitive to ion and electron temperature assumptions. The measured line strengths fall more slowly with increasing order than the theoretical line strengths, indicating that these lines are still optically thick.

The magnitude of the temperature discrepancies (Table 5-3) suggest that the temperature in the radiating core has a steep radial gradient, which makes it difficult to perform simple estimates of the peak plasma density and temperature from the line ratios. Instead one must find a unique profile that provides a good match to all the spectral features (preferably time-resolved). Apruzese
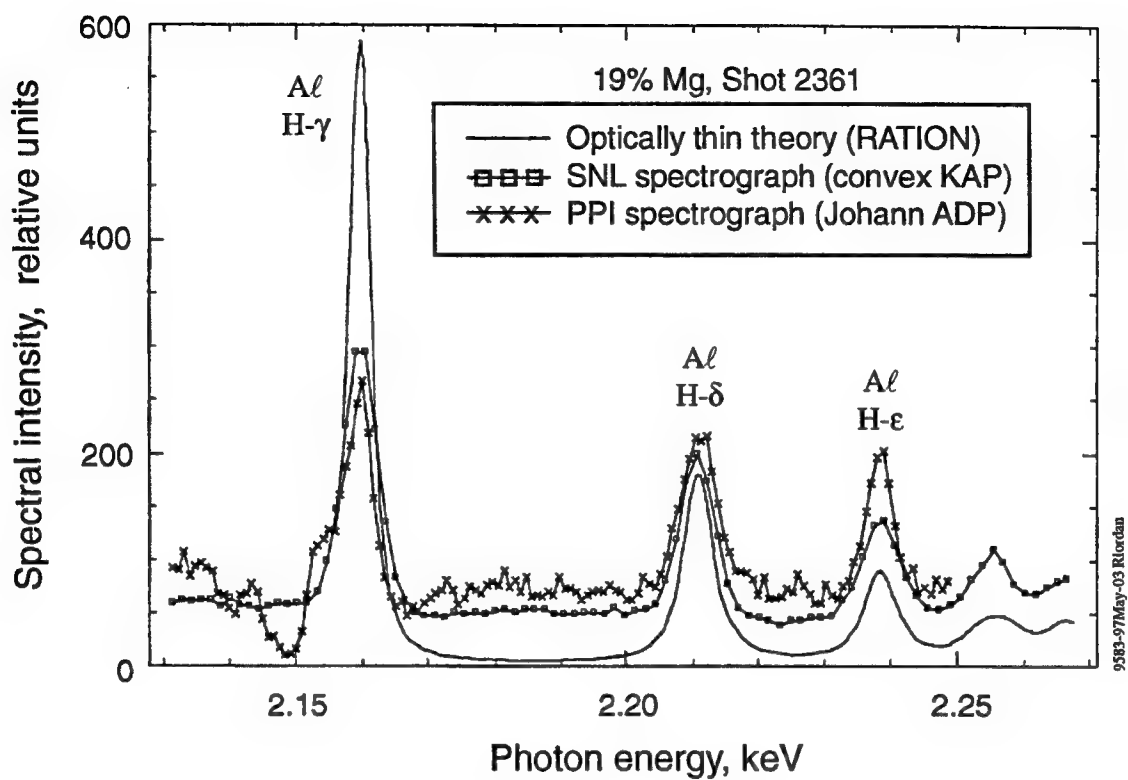
Figure 5-6. Comparison H-like aluminum lines in measured and optically-thin calculated spectra.

has reconciled the time-integrated spectral data using a temperature profile that peaked at 2.6 keV on axis and fell by a factor of four at a 3-mm radius (Reference 15). At this peak temperature the aluminum and magnesium ions are completely stripped, which can explain the fact that the Saturn x-ray yields did not exceed those of Double-EAGLE despite the 67% increase in load mass.

5.4 ALUMINUM/POTASSIUM CHLORIDE RESULTS.

The addition of potassium chloride to the aluminum wires was intended to increase the x-ray yield in the spectral range containing the chlorine and potassium He-α lines at 2.8 and 3.5 keV, respectively. As expected, the potassium chloride coating increased the yield above 2.7 keV, but only slightly (Table 5-2). The major effect of the potassium chloride coating, however, was a significant decrease in the combined K-shell x-ray yield. Figure 5-4 shows that the yield decrease was nearly proportional to the coating mass fraction. A similar effect was observed using titanium-coated aluminum wires on Double-EAGLE, where 18% Ti wires produced a 33% decrease in the total K-shell yield. Since the total radiated yield increased somewhat with the potassium chloride mass fraction (Table 5-2), it seems highly probable that much of the plasma energy was radiated in potassium and chlorine L-shell lines below 1 keV.

The time-integrated K-shell spectra of Figure 5-7 can help explain the minimal increase in yield above 2.7 keV. These spectra show that the potassium and chlorine ions are primarily He-like, with lesser amounts of Li-like. Nevertheless, the x-ray yield above 2.7 keV comes not only from the potassium and chlorine 1s-2p lines, but also from the intense aluminum free-bound continuum. Although the line radiation increased with the coating mass fraction, the increased yield was nearly offset by a decrease in the aluminum continuum. The aluminum/titanium and argon/titanium mixtures on Double-EAGLE, however, did show a significant yield increase in the titanium K-shell spectral range, because the aluminum and argon free-bound continua were nearly negligible in this higher spectral range.
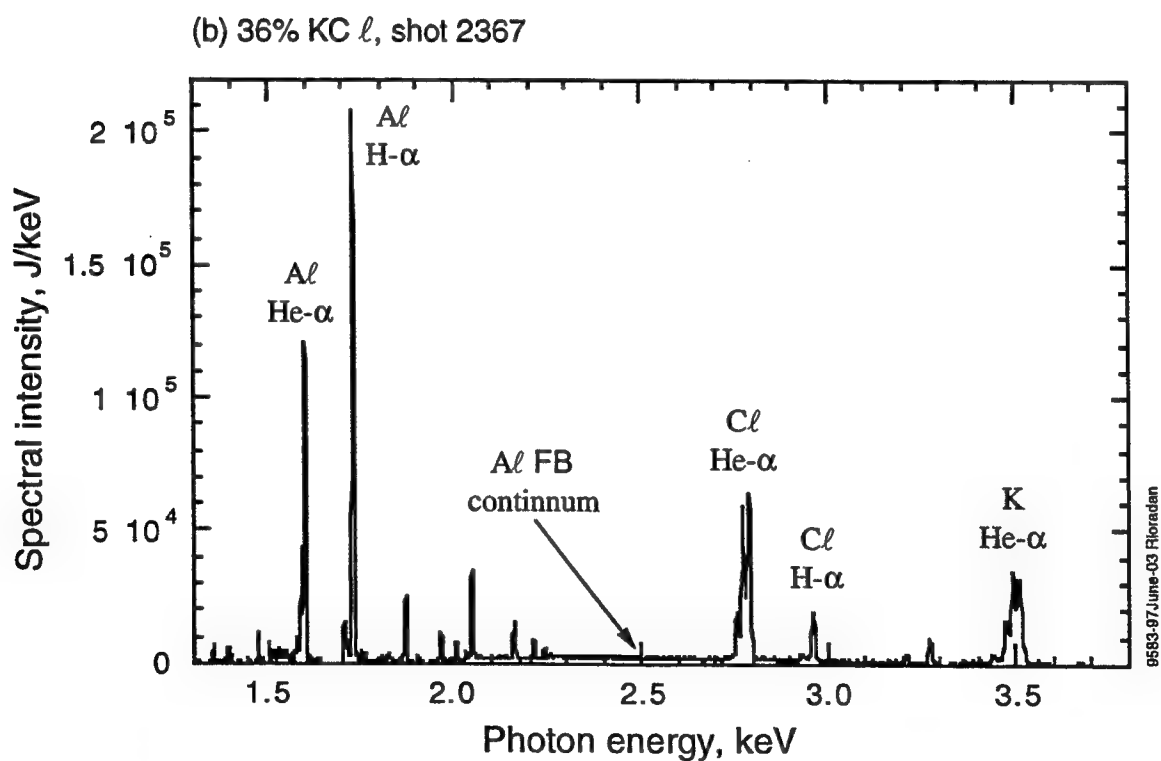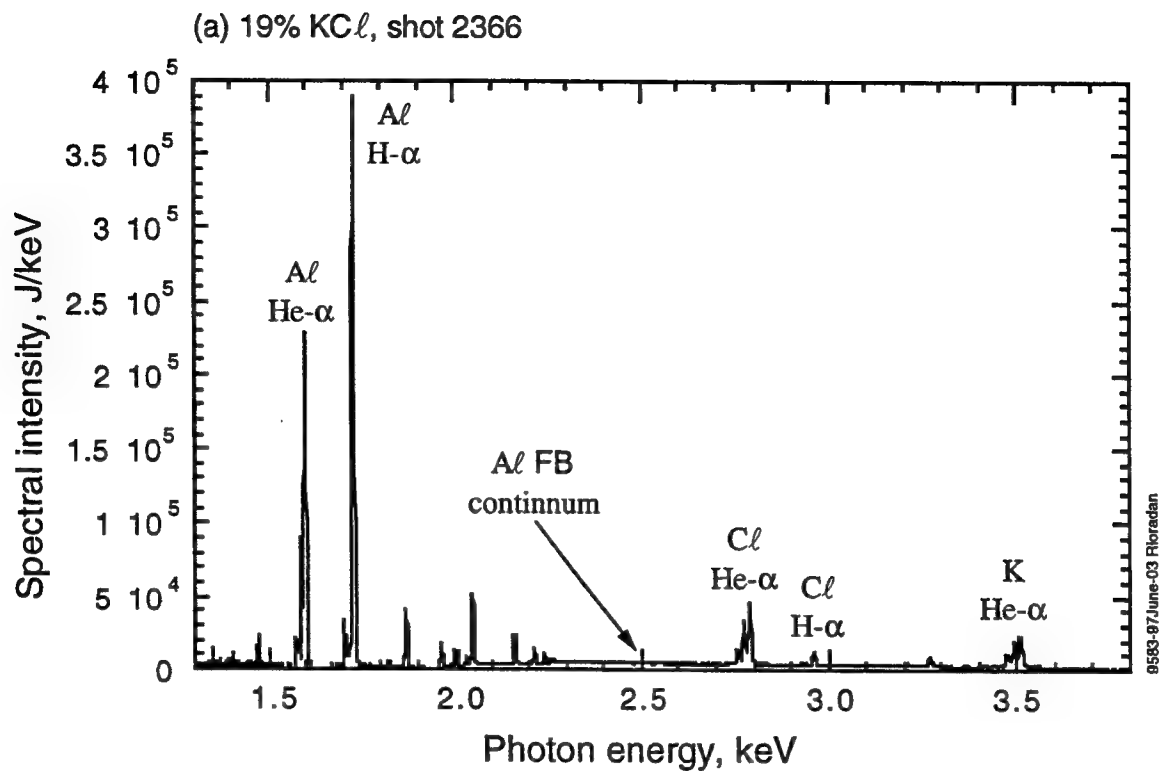
Figure 5-7. Measured spectra for aluminum wires with potassium chloride coating; (a) 19% KCl and (b) 36% KCl.

SECTION 6

REFERENCES

1. K. G. Whitney et al., Phys. Rev. E50, 2166 (1994) (UNCLASSIFIED).

2. J. Katzenstein, J. Appl. Phys. 52, 767 (1981) (UNCLASSIFIED).

3. T. W. L. Sanford et al, Proc. 11th Intl. Conf. High Power Particle Beams, 146 (1996) (UNCLASSIFIED).

4. C. Deeney et al, Phys. Rev A 44, 6762 (1991) (UNCLASSIFIED).

5. D. Mosher, Proc. 10th Intl. Conf. High Power Particle Beams, 159 (1994) (UNCLASSIFIED).

6. J. P. Apruzese and J. Davis, J. Appl. Phys. 57, 4349 (1985) (UNCLASSIFIED).

7. C. Deeney et al., Phys. Rev. E51, 4823 (1995) (UNCLASSIFIED).

8. J. W. Thornhill et al., Naval Research Laboratory Report NRL/MR/6720-96-7735, 26 (1996) (UNCLASSIFIED).

9. P. D. LePell et al., GOMAC/HEART Conf. Digest of Papers v. 21, 584 (1996) (UNCLASSIFIED).

10. J. W. Thornhill et al., Naval Research Laboratory Report NRL/MR/6720-96-7802, 48 (1996) (UNCLASSIFIED).

11. J. Apruzese, private communication (UNCLASSIFIED).

12. F. J. Wessel et al., J. Appl. Phys. (to be published) (UNCLASSIFIED).

13. M. C. Coulter et al., J. Quant. Spectrosc. Radiat. Transfer 44, 443 (1990) (UNCLASSIFIED).

14. P. L'Eplattenier, private communication (UNCLASSIFIED).

15. J. Apruzese et al., IEEE Trans. Plasma Sci. (to be published) (UNCLASSIFIED).

DISTRIBUTION LIST

DEPARTMENT OF DEFENSE

BALLISTIC MISSILE DEFENSE OFFICE
7100 DEFENSE PENTAGON
WASHINGTON, D.C. 20301-7100
    ATTN: T/SL

DEFENSE ADVANCED RESEARCH
PROJECTS AGENCY
3701 NORTH FAIRFAX DRIVE
ARLINGTON, VA 22203-1714
    ATTN: DED

COMMANDER
DEFENSE INFORMATION SYSTEMS
AGENCY, PACIFIC AREA
WHEELER AFB, HI 96854-5000
    ATTN: COMMANDER

DEFENSE TECHNICAL INFORMATION CENTER
8725 JOHN J. KINGMAN ROAD, SUITE 0944
FORT BELVOIR, VA 22060-6218
    ATTN: DTIC/OCP

DEFENSE THREAT REDUCTION AGENCY
6801 TELEGRAPH ROAD
ALEXANDRIA, VA 22310-3398
    ATTN: CPF
    ATTN: CPF, P. HEBERT
    ATTN: CPWCT
    ATTN: CPWP, T. KENNEDY
    ATTN: CPWT
    ATTN: NSC
    ATTN: NSS, J. M. PIERRE
    ATTN: NSSA, DR G. DAVIS
    ATTN: NSSA, W. SUMMA
    ATTN: NSSE, W. J. SCOTT
    ATTN: NSSS, D. BELL
    ATTN: NSSS, DR K. WARE
    ATTN: NSSS, L. PRESSLEY
    ATTN: NSSS, R. GULLICKSON
    ATTN: NSSS, R. SCHNEIDER
    ATTN: NSSS, R. MAINGER
    ATTN: SWWA

DEFENSE THREAT REDUCTION AGENCY
ALBUQUERQUE OPERATIONS
1680 TEXAS STREET, SE
KIRTLAND AFB, NM 87117-5669
    ATTN: CPT D, DR G. BALADI
    ATTN: CPTO
    ATTN: CPTO, R. W. SHOUP

PRESIDENT
NATIONAL DEFENSE UNIVERSITY
FORT LESLEY J. MCNAIR
WASHINGTON, DC 20319-6000
    ATTN: NWCO

DIRECTOR
NET ASSESSMENT
OFFICE OF THE SEC OF DEFENSE
ROOM 3A930, THE PENTAGON
WASHINGTON, DC 20301
    ATTN: DOCUMENT CONTROL

DEPARTMENT OF DEFENSE CONTRACTORS

AEROSPACE CORP
P. O. BOX 92957
LOS ANGELES, CA 90009
    ATTN: LIBRARY ACQUISITION M1/199
    ATTN: M2/241, T. PARK

ALME AND ASSOCIATES
ATTN: DOC
P. O. BOX 4057
ALEXANDRIA, VA 22303
    ATTN: J. F. DAVIS
    ATTN: S. SEILER, G101

APTEK, INC.
1257 LAKE PLAZA DRIVE
COLORADO SPRINGS, CO 80906-3578
    ATTN: T. MEAGHER

BERKELEY RESEARCH ASSOCIATES, INC.
P. O. BOX 852
SPRINGFIELD, VA 22150-0852
   ATTN: N. PEREIRA

CHARLES STARK DRAPER LAB, INC.
555 TECHNOLOGY SQUARE
CAMBRIDGE, MA 02139
   ATTN: LIBRARY, MS #74

DEFENSE GROUP, INC.
P. O. BOX 7522
SANTA MONICA, CA 90406-7522
   ATTN: R. POLL
   ATTN: MAIL STOP 3,
      TECH INFO CTR

HY-TECH RESEARCH CORPORATION
104 CENTRE COURT
RADFORD, VA 24141
   ATTN: E. J. YADLOWSKY

E-SYSTEMS, INC.
ECI DIVISION
P. O. BOX 12248
ST PETERSBURG, FL 33733-2248
ATTN: MAIL STOP 3, TECH INFO CTR

ITT INDUSTRIES
ITT SYSTEMS CORPORATION
ATTN: AODTRA/DASIAC
1680 TEXAS ST, SE
KIRTLAND AFB, NM 87117-5669
   ATTN: DASIAC
   ATTN: DASIAC/DARE

ITT SYSTEMS CORPORATION
2560 HUNTINGTON AVENUE
ALEXANDRIA, VA 22303
   ATTN: C. FORE

JAYCOR
1410 SPRING HILL ROAD, SUITE 300
MCLEAN, VA 22102
   ATTN: DR C. P. KNOWLES

JAYCOR
P. O. BOX 85154
SAN DIEGO, CA 92186-5154
   ATTN: M. TREADAWAY

KTECH CORPORATION
2201 BUENA VISTA DRIVE, SE, SUITE 400
ALBUQUERQUE, NM 87106-4265
   ATTN: F. DAVIES

LOGICON - RDA
2100 WASHINGTON BOULEVARD
ARLINGTON, VA 22204-5706
   ATTN: E. QUINN
   ATTN: I. VITKOVITSKY

MAXWELL PHYSICS INT'L CO.
2700 MERCED STREET
SAN LEANDRO CA 94577-0599
   ATTN: B. FAILOR
   ATTN: C. STALLINGS
   ATTN: J. RIORDAN
   ATTN: P. SINCERNY
   ATTN: S. L. WONG

MAXWELL TECHNOLOGIES
8888 BALBOA AVENUE, BUILDING 1
SAN DIEGO, CA 92123
   ATTN: J. THOMSON
   ATTN: P. COLEMAN
   ATTN: W. H. RIX

MISSION RESEARCH CORPORATION
1720 RANDOLPH ROAD, SE
ALBUQUERQUE, NM 87106-4245
   ATTN: K. STRUVE

PRIMEX PHYSICS INTERNATIONAL
P O BOX 5010
SAN LEANDRO, CA 94577-0599
   ATTN: B. H. FAILOR
   ATTN: C. A. COVERDALE
   ATTN: C. DEENEY
   ATTN: J. C. RIORDAN
   ATTN: P. D. LEPELL

PULSE SCIENCES, INC.
600 MC CORMICK STREET
SAN LEANDRO, CA 94577
   ATTN: I. D. SMITH
   ATTN: P. W. SPENCE
   ATTN: TECHNICAL LIBRARY

SCIENCE APPLICATIONS INT'L CORPORATION
P. O. BOX 1303
MCLEAN, VA 22102
   ATTN: W. CHADSEY

SRI INTERNATIONAL
333 RAVENSWOOD AVENUE
MENLO PARK, CA 94025-3434
   ATTN: ELECTROMAG SCI LAB
      TECH LIB

SVERDRUP INC AEDC
253 1ST STREET
ARNOLD AFB, TN 37389-2250
    ATTN: L. S. CHRISTENSEN, MS 640

SVERDRUP TECHNOLOGY INC.
P. O. BOX 884
TULLAHOMA, TN 37388
    ATTN: V. KENYON

TEXAS TECH UNIVERSITY
PULSED POWER LABORATORY
PHYSICS DEPARTMENT
LUBBOCK, TX 79409
    ATTN: L. HATFIELD, M/S 1051
    ATTN: M. KRISTIANSEN, M/S 3102

DEPARTMENT OF ENERGY

US ARMY SPACE & STRATEGIC
DEFENSE COMMAND
CSSD-TC-SR
P. O. BOX 1500
HUNTSVILLE, AL 35807-3801
    ATTN: CSSD-ES-E1, R. CROWSON

US ARMY THAAD PROJECT OFFICE
P. O. BOX 1500
HUNTSVILLE, AL 35807-3801
    ATTN: CSSD-WD

COMMANDER
US ARMY VULNERABILITY
ASSESSMENT LAB
WHITE SANDS MISSILE RANGE,
NM 88002-5513
    ATTN: SLCVA-TAC

DEPARTMENT OF THE NAVY

COMMANDER
NAVAL AIR SYSTEMS COMMAND
47123 BUSE ROAD, #IPT
PATUXENT RIVER, MD 20670
    ATTN: AIR 5161
    ATTN: AIR-5164
    ATTN: AIR-933

NAVAL RESEARCH LABORATORY
4555 OVERLOOK AVENUE, SW
WASHINGTON, DC 20375-5000
    ATTN: CODE 6720, J. DAVIS
    ATTN: CODE 6770, G. COOPERSTEIN

COMMANDER
NAVAL SURFACE WARFARE CENTER
DAHLGREN DIVISION
17320 DAHLGREN ROAD
DAHLGREN, VA 22448-5000
    ATTN: B. DEPARTMENT

OFFICE OF NAVAL INTELLIGENCE
4251 SUITLAND ROAD
WASHINGTON, DC 20395-5720
    ATTN: DEOO
    ATTN: LIBRARY

COMMANDER
SPACE & NAVAL WARFARE SYS CMD
DEPARTMENT OF THE NAVY
2451 JEFFERSON-DAVIS HIGHWAY
ARLINGTON, VA 22245
    ATTN: PMW-145

DIRECTOR
STRATEGIC SYSTEMS PROGRAMS
37224 TRIDENT
1931 JEFFERSON DAVIS HIGHWAY
ARLINGTON, VA 22202-5362
    ATTN: J. BURTLE
    ATTN: K. TOBIN

OTHER GOVERNMENT

CENTRAL INTELLIGENCE AGENCY
WASHINGTON, DC 20505
    ATTN: OSWR, J. PINA
    ATTN: OSWR/SSD/SWB
    ATTN: OSWR/STD/TTB

FEDERAL EMERGENCY MANAGEMENT AGENCYY
500 C. STREET, SW, SUITE 514
WASHINGTON, D.C. 20472
    ATTN: SL-CD-MP

DIRECTOR
NATIONAL SECURITY AGENCY
FORT GEORGE G. MEADE, MD
20755-6000
    ATTN: TECHNICAL LIBRARY